NFκB nuclear dynamics orchestrate inflammatory aging

Sho Tabata[1], Keita Matsuda[1], Kenshiro Nagai[1], Yoshihiro Izumi[2], Masatomo Takahashi[2], Yasutaka Motomura[3,4,5], Ayaka Ichikawa Nagasato[1], Shuichi Shimma[6], Kazuyo Moro[3,4,5,7], Takeshi Bamba[2], Mariko Okada[1,8]*

[1] Laboratory for Cell Systems, Institute for Protein Research, Osaka University; Suita, Osaka, 565-0871, Japan.

[2] Division of Metabolomics/Mass Spectrometry Center, Medical Research Center for High Depth Omics, Medical Institute of Bioregulation, Kyushu University; Fukuoka, Fukuoka, 812-8582, Japan.

[3] Laboratory for Innate Immune Systems, Department of Microbiology and Immunology, Graduate School of Medicine, Osaka University; Suita, Osaka 565-0871, Japan.

[4] Laboratory for Innate Immune Systems, Immunology Frontier Research Center (IFReC), Osaka University; Suita, Osaka, 565-0871, Japan.

[5] Laboratory for Innate Immune Systems, RIKEN Center for Integrative Medical Sciences (IMS); Yokohama, Kanagawa 230-0045, Japan.

[6] Department of Biotechnology, Graduate School of Engineering, Osaka University; Suita, Osaka, 565-0871, Japan.

[7] Laboratory for Innate Immune Systems, Graduate School of Frontier Biosciences, Osaka University; Suita Osaka, 565-0871, Japan.

[8] Premium Research Institute for Human Metaverse Medicine (WPI-PRIMe), Osaka University; Suita Osaka, 565-0871, Japan.

*Corresponding author. Email: mokada@protein.osaka-u.ac.jp

Abstract

Upregulation of nuclear factor κB (NFκB) signaling is a hallmark of aging and a major cause of age-related chronic inflammation. NFκB activity plays a critical role in transcriptional regulation and cell fate determination; however, its physiological function in inflammatory aging remains unclear. Here, we demonstrate that dysfunction of negative feedback regulators of NFκB, IκBα and A20, alters the NFκB nuclear dynamics from oscillatory to sustained, thereby promoting cellular senescence. Sustained NFκB activity by IκBα downregulation enhances inflammatory gene expression through increased NFκB-DNA binding, promotes purine catabolism by downregulating hypoxanthine phosphoribosyltransferase, and arrests the cell cycle. This regulatory mechanism was confirmed in aged mice heart tissues, suggesting that prolonged nuclear localization of NFκB drives chronic inflammation and metabolic rewiring associated with aging.

Main

Aging is a complex and irreversible phenomenon that reflects lifelong biochemical responses to the environment. Recent research has provided evidence for age-related dysfunction from the genome to organ levels [1, 2]. Inflammatory aging, which refers to aging-associated chronic inflammation, critically impacts the induction of a wide range of age-related human diseases [3], and its regulation is becoming increasingly important in aging societies. In particular, elderly individuals exhibit low-level of chronic inflammation in their tissues along with elevated levels of circulating inflammatory factors such as interleukin-6 and tumor necrosis factor alpha (TNFα) that activate nuclear factor κB (NFκB) signaling [4, 5]. Meanwhile, the accumulation of senescent cells during aging produces various pro-inflammatory cytokines known as senescence-associated secretory phenotype (SASP), which increases the risk of developing age-related diseases [6]. Since NFκB is the master transcription factor for SASP genes [7], NFκB acts as a positive feedback regulator in aging and cellular senescence. However, several studies have also shown that NFκB prevents cellular senescence [8, 9]. Therefore, we speculate that quantitative rather than qualitative understanding of NFκB activity is necessary to unravel the role of NFκB in cellular senescence and inflammatory aging.

NFκB regulates the expression of genes involved in immune responses, proliferation, apoptosis, and cellular senescence [7, 10, 11]. Excessive NFκB activity induces pathological inflammation and contributes to the progression of various human diseases [7, 12]. Notably,

NFκB also induces transient, sustained, or oscillatory nuclear dynamics which are associated with different biological functions and cell fates [13]. For example, the quantitative features of NFκB activity including peak amplitude, duration, speed, and oscillation are associated with the discrimination of immune threats in macrophages [14] and it encodes the short-term history derived from prior pathogenic and cytokine signals, affecting later cell functions [15]. These studies demonstrate that homeostasis of NFκB nuclear dynamics is important for maintenance of cellular functions.

The canonical NFκB pathway undergoes negative feedback regulation in response to environmental factors and exhibits stimulus-specific oscillatory dynamics. In particular, NFκB inhibitor alpha (IκBα), which is rapidly expressed upon NFκB activation, acts as a strong negative feedback regulator and induces characteristic NFκB oscillatory patterns [16]. Notably, knockout (KO) or knockdown (KD) of the IκBα gene in TNFα-stimulated cells results in sustained NFκB nuclear activation and upregulation of immediately expressed genes that show distinct patterns generated from oscillatory NFκB [17-19]. However, the physiological significance of NFκB activity dynamics and its long-term implications are yet to be fully addressed. Therefore, we investigated the impact of the changes in TNFα-induced NFκB dynamics in relation to cellular senescence. First, we confirmed that IκBα KD altered the oscillatory NFκB nuclear activity to sustained activity in MCF-7 cells stimulated with TNFα (Fig. 1a and Extended Data Fig 1a,b). The change in NFκB dynamics suppressed cell proliferation (Fig. 1b), flattened cell shape, and significantly increased cell size (Fig. 1c and Extended Data Fig. 1c,d), features that are similar to the senescence phenotype [20]. Therefore, we examined SA-β-gal activity, one of the indicators of cellular senescence [21]. Although TNFα alone did not promote SA-β-gal activity, under IκBα KD/KO conditions, TNFα increased the number of SA-β-gal positive cells (Fig. 1d and Extended Data Fig. 1e–g). The number of SA-β-gal positive cells was suppressed by KD of RELA, a subunit of NFκB, in IκBα KD+TNFα conditions (Extended Data Fig. 2a–c), confirming that the phenomenon is NFκB-dependent. As senescent cells typically exhibit SASP [6, 21], we next examined its effect under IκBα KD+TNFα conditions. The expression of various SASP genes, including *IL8* and *CCL2* was drastically elevated (Fig. 1e and Extended Data Fig. 2d). Furthermore, cell cycle analysis using FUCCI live cell imaging revealed that IκBα KD+TNFα induced cell arrest at G2/M phase (Fig. 1f and Extended Data Fig. 2e,f) and downregulated the expression of the cell cycle promoter Cyclin D1 (Fig. 1g) compared with that in TNFα alone. These results indicate

that sustained NFκB activity mimicked by IκBα KD+TNFα promotes cellular senescence.

Next, we addressed whether the sustained NFκB dynamics, rather than IκBα itself, were responsible for the induction of cellular senescence. In addition to IκBα, A20 acts a negative feedback regulator of the NFκB pathway, and its downregulation results in sustained NFκB dynamics [22, 23]. Therefore, we investigated whether A20 KD promotes cellular senescence and found that A20 KD+TNFα increased SA-β-gal staining and expression of SASP genes (*IL8* and *CCL2*) and slightly reduced Cyclin D1 expression (Fig. 2a–c and Extended Data Fig. 2g,h); however, these effects were smaller than those of IκBα KD (Fig. 1d–g). To evaluate the quantitative difference of IκBα and A20 effects on NFκB nuclear dynamics, we constructed a mathematical model of the NFκB pathway (Fig. 2d, Extended Data Fig. 3a and Supplementary Tables 1–3) modified from earlier studies [24, 25] and performed simulation analysis. We trained the model with time-course data obtained from TNFα-stimulated MCF-7 cells (Extended Data Fig. 3b–d) and analyzed altered NFκB dynamics by IκBα and A20 KD. Simulation analysis with downregulation or overexpression (OE) of IκBα or A20 showed that IκBα has a larger effect on the duration and total abundance of nuclear NFκB activity (Fig. 2e, Extended Data Fig. 4a–d). Sensitivity analysis (see the Methods) also confirmed the slightly higher sensitivity of IκBα-related reactions than that of A20 to the sum of nuclear NFκB activity (Extended Data Fig. 4e). The result was consistent with the experimental results of NFκB nuclear dynamics (Fig.1a, Fig. 2f, and Extended Data Fig. 5a) and cellular senescent phenotypes (Fig. 1d,e,g and Fig. 2a–c) compared between IκBα and A20 KD. Furthermore, we assessed whether A20 OE could compensate for the effect of IκBα downregulation, and performed a simulation of nuclear NFκB dynamics by combining IκBα KD and A20 OE (Fig. 2g and Extended Data Fig. 5b). Under A20 OE, IκBα KD exhibited sustained NFκB activity dynamics, however, its overall amplitude was reduced. To confirm the simulation results experimentally, we established A20 OE MCF-7 cells (Extended Data Fig. 5c) and examined the effect of IκBα KD on NFκB dynamics. A20 OE reduced the amplitude of sustained NFκB activity in IκBα KD+TNFα conditions as computationally predicted (Fig. 2h and Extended Data Fig. 5d) and could not recover the number of SA-β-gal positive cells and SASP gene expression (Fig. 2i,j). These results suggested that the total sum of nuclear NFκB activity might be associated with the degree of cellular senescence.

We next investigated the relationship between NFκB nuclear dynamics and target gene regulation. First, we extracted differentially expressed genes (DEGs) in MCF7 cells under IκBα KD+TNFα (48 hr) conditions that exhibited a cellular senescence phenotype (vs. TNFα), and identified 687 upregulated DEGs, including cellular senescence-promoting and SASP genes (e.g., *CD36*, *BCL3*, *CCL2*, and *S100A8*/*A9*) [1, 21, 26, 27] (Extended Data Fig. 6a). These genes then classified into four clusters based on the time-course patterns of gene expression which was measured every 15 min in the IκBα KD+TNFα condition in MCF-7 cells [17] (Fig. 3a). To clarify whether the gene expression time-course is associated with chromatin status, chromatin accessibility was assessed using an assay for transposase-accessible chromatin sequencing (ATAC-seq) data. We found that the ATAC signal was elevated in the flanking regions of genes in cluster 2, which showed a monotonically increasing pattern, and their signal was stronger in the IκBα KD+TNFα condition (Fig. 3b). Considering that the chromatin accessibility enhanced by IκBα KD+TNFα might be critical for gene regulation under sustained nuclear NFκB activity, we extracted the regions where chromatin accessibility was significantly enhanced by IκBα KD+TNFα (Extended Data Fig. 6b) and assessed the NFκB binding to these regions. We analyzed NFκB (RELA)-chromatin immunoprecipitation sequencing (ChIP-seq) data and found that the RELA signal intensity in chromatin open regions proximal to cluster 2 genes was significantly increased under IκBα KD+TNFα conditions, but not under the condition with TNFα alone (Fig. 3c). Furthermore, we investigated whether quantitative differences in the number of NFκB binding sites affected the regulation of gene expression for each cluster (Fig. 3d). Notably, the average number of RELA binding sites in cluster 2 was significantly higher than that for all NFκB target genes. Since cluster 2 genes were enriched with cytokine signaling pathways (Extended Data Fig. 6c), these results suggest that sustained nuclear NFκB localization contributes to the upregulation of cytokine signaling by increasing NFκB binding to their regulatory regions.

Senescent cells accumulate at sites of aging-related diseases and in aged tissues in a variety of mammals [21]. Given that sustained NFκB activity may be involved in the progression of cellular senescence and chronic inflammation associated with aging *in vivo*, we examined the levels of IκBα, A20, and TNFα in young (8-weeks-old) and aged (69–73-weeks-old) mice. We found decreased expression of IκBα and A20 proteins and increased TNFα in several tissues of aged mice (Fig. 3e,f and Extended Data Fig. 6d,e). In particular, IκBα ($P < 0.01$, FC = 0.622, vs. young hearts) and A20 ($P < 0.01$, FC = 0.6092, vs. young hearts) expression was decreased and TNFα ($P < 0.01$, FC = 1.356, vs.

young hearts) expression was increased in the hearts of aged mice. Thus, we investigated the gene expression in hearts from young and aged mice using RNA-seq. Prediction of active transcription factors using DoRothEA [28] suggested that NFκB family members, NFKB1 and RELA, were activated in aged heart tissues (Extended Data Fig. 7a). The fold change relationship between genes with sustained NFκB activity *in vitro* (IκBα KD+TNFα vs. control MCF-7) and those with aging *in vivo* (aged vs. young mice) in the mouse heart revealed that the expression of cluster 2 genes (Fig. 3a), including cellular senescence-promoting and SASP genes, was correlated with the age-related gene expression in the heart (R = 0.31, $P < 0.0001$) but not other clusters (Fig. 3g). In addition, we examined the relationship between the number of NFκB binding sites and the increase in gene expression with aging in the mouse heart. After predicting putative NFκB targets using the ChIP-Atlas [29] (see the Methods), we classified the genes into four groups (no, low, medium, and high upregulation) according to the degree of fold change expression with aging (aged vs. young mice) (Extended Data Fig. 7b). Counting NFκB binding sites in the flanking regions of the genes using HOMER [30] revealed that the "high" expression group included a significantly larger number of NFκB binding motifs ($P < 0.0001$, High vs. no upregulation) (Fig. 3h). Gene Ontology (GO) analysis of the high group genes in the aging heart (Fig. 3i) revealed a high enrichment of inflammatory signals, similar to the GO of the cluster 2 gene set in MCF-7 cells (Extended Data Fig. 6c). These results strongly support the hypothesis that NFκB accumulates in the nucleus *in vivo*, and in fact, our histochemical experiments found a marked increase in NFκB-positive cells in the nuclei of aged hearts (Extended Data Fig. 7c).

Next, we analyzed the changes in the signaling and downstream cascade induced by sustained NFκB activation and the relationship with cellular senescence. We focused on the decreased expression of Cyclin D1 by IκBα KD+TNFα (Fig. 1g). Expression of Cyclin D1 is regulated by multiple signaling pathways [31], therefore we examined the effect of several pathway inhibitors (Extended Data Fig. 8a,b). AKT Inhibitor VIII (AKTi-VIII; AKT1/2 inhibitor), SB203580 (inhibitor for p38 and AKT), and BAY-117085 (NFκB inhibitor) abrogated the changes in Cyclin D1 expression in IκBα KD+TNFα conditions (Extended Data Fig. 8b). Given that sustained NFκB activity is implicated in AKT activation, we analyzed the signaling pathway involved in AKT and found that the expression of RICTOR, P-RICTOR, and P-AKT (Ser473) in the mTOR complex 2 (mTORC2) cascade was significantly reduced by IκBα KD+TNFα (Fig. 4a and Extended Data Fig. 8c). Moreover, RICTOR KD and AKTi-VIII treatment

increased SA-β-gal staining and decreased Cyclin D1 expression in MCF-7 cells (Extended Data Fig. 8a,d,e). AKTi-VIII also abolished the effect of IκBα KD+TNFα on SA-β staining (Extended Data Fig. 8f). These results suggested that IκBα KD-induced sustained NFκB activity suppresses mTORC2 signaling.

mTORC2 is a critical factor in metabolic regulation [32]. Since metabolic dysregulation is a hallmark of cellular senescence and aging [21], we investigated the metabolic alteration induced by sustained NFκB activation. We performed metabolome analysis of MCF-7 cells under IκBα KD+TNFα conditions; however, the principal component analysis showed similar intracellular metabolic profiles between TNFα and IκBα KD+TNFα (Extended Data Fig. 9a and Supplementary Data S1). TNFα alters several metabolic pathways, including glycolysis, lipid metabolism, and amino acid metabolism [33-35], which might mask metabolic changes associated with cellular senescence in IκBα KD+TNFα conditions. Since IκBα KD alone reduced mTORC2 activity moderately (Fig 4a and Extended Data Fig. 8c), we focused on the metabolic alteration induced by IκBα KD. The results showed that 62 and 35 metabolite levels were up- and down-regulated, respectively (Fig. 4b). Notably, the intracellular level of hypoxanthine in the purine catabolic pathway was significantly elevated by IκBα KD ($P < 0.0001$, FC = 3.126, vs. control), and its effects were enhanced by TNFα ($P < 0.0001$, FC = 4.711, vs. control) (Fig. 4b,c). Extracellular hypoxanthine level in the culture medium was also increased by IκBα KD+TNFα ($P < 0.0001$, FC = 17.69, vs. control) (Extended Data Fig. 9b,c). Pathway enrichment analysis of metabolites altered by IκBα KD also confirmed the global changes in the purine metabolic pathway (Fig. 4d). Mapping of intracellular metabolite changes induced by IκBα KD showed an increase in metabolites of the catabolic pathway (e.g., hypoxanthine, xanthine) and a decrease in high energy molecules (e.g., ATP and GTP) (Fig. 4e). Detailed analysis of mRNA and protein levels in IκBα KD cells validated promotion of purine catabolism, including increased ecto-5'-nucleotidase (NT5E) or decreased hypoxanthine phosphoribosyltransferase (HPRT) 1 levels, which were enhanced by TNFα (Fig. 4f and Extended Data Fig. 9d). To address whether purine catabolism is involved in the progression of cellular senescence, we next tested the effect of NT5E and HPRT1 inhibition. NT5E inhibitor, adenosine 5'-(α, β-methylene) diphosphate (APCP), attenuated the increased SA-β-gal positive cells by IκBα KD+TNFα, whereas siRNA-mediated HPRT1 KD augmented SA-β-gal staining (Fig. 4g and Extended Data Fig. 9e,f). Furthermore, RICTOR knockdown decreased HPRT1 expression, but did not affect NT5E expression (Extended Data Fig. 9g), suggesting that IκBα KD+TNFα decreased HPRT1 expression

via RICTOR. MCF-7 cells under IκBα KD+TNFα conditions show cell cycle arrest in G2/M phase (Fig. 1f), which may be due to the depletion of DNA/RNA building blocks such as ATP, GTP, dATP, and dGTP by purine catabolism. These results indicated that sustained NFκB activation rewires metabolic pathways to enhance purine catabolism and promotes cellular senescence by inhibiting *de novo* DNA/RNA synthesis and cell cycle progression.

We next examined whether purine catabolism by sustained NFκB activation is also observed in the hearts of aged mice *in vivo*. Protein expression of RICTOR and HPRT in aged hearts was significantly lower than that in young hearts (Extended Data Fig. 10a,b), and HPRT levels were correlated with IκBα levels in young and aged hearts ($R = 0.7676$, $P < 0.001$) (Fig. 4h). Metabolome analysis of the hearts of aged mice revealed enhanced purine catabolic metabolism (Fig. 4i,j and Supplementary Data 2), similar to that of the MCF-7 cells under IκBα KD+TNFα conditions. Interestingly, mass spectrometry imaging revealed that ATP levels in the hearts of aged mice were markedly reduced in the entire tissue (Fig. 4k and Extended Data Fig. 10c).

The duration of nuclear NFκB activity has a variety of effects on gene expression by regulating mRNA half-life or epigenetic status [18, 19]. In this study, we show that sustained NFκB activity in proinflammatory conditions drives cellular senescence by affecting cell morphology, cell cycle arrest, SASP induction and SA-β-gal staining. The aging-associated phenotypic changes could be explained by a core regulatory mechanism stemming from sustained nuclear NFκB activity, that increases NFκB-DNA binding for inflammatory gene expression, alters the mTORC2-AKT pathway, and promotes purine catabolism to reduce DNA synthesis and cell cycle progression. Hypoxanthine, which is significantly elevated in the IκBα KD+TNFα condition, is a common DNA damage base [36]. Therefore, it may contribute to accelerating the aging process by depleting normal cell functions. Our study showed that the loss of two negative feedback regulators, that is, IκBα and A20, significantly elevated the nuclear abundance of NFκB and induction of cell senescence, indicating that appropriate control of the duration of nuclear NFκB activity is critical for prevention of inflammatory aging. Indeed, the decrease in IκBα protein levels under oxidative stress in MCF-7 cells (Extended Data Fig. 10d) indicates that decreases in IκBα in aged tissues may occur over a lifetime for the same reason. Meanwhile, previous studies have demonstrated that defects in the feedback regulation of IκBα in the NFκB pathway cause Sjögren's syndrome and shortened life span [37], while mice expressing vascular-specific IκBα

overexpression have a prolonged life span [38]. However, further studies are needed to determine how sustained NFκB activity by IκBα downregulation decreased RICTOR expression and enhanced purine catabolism. Notably, inhibition of purine nucleoside phosphorylase, one of the rate-limiting enzymes for purine catabolism, suppresses cellular senescence *in vivo*, ameliorates age-associated lower urinary tract dysfunction [39], and promotes the synthesis of nicotinamide adenine dinucleotide, an anti-ageing molecule [40]. In this study, we show that temporal NFκB dynamics affect an unexpectedly broad spectrum of cell physiology and regulate cellular senescence, which provides unprecedented insight into the molecular basis of cellular senescence.

Methods

Reagents and cell culture

TNFα was purchased from Thermo Fisher Scientific (Waltham, MA, USA). MG132, Rapamycin, and LY294002 were purchased from Calbiochem (Merck Millipore, Burlington, MA, USA), BAY11-7085 was purchased from Fujifilm Wako Pure Chemical Industries, Ltd. (Osaka, Japan). AKT inhibitor VIII was purchased from Cayman Chemical (Ann Arbor, MI, USA). SB216763 was purchased from Sigma-Aldrich (St Louis, MO, USA). SB203580 was purchased from Cell Signaling Technology (Danvers, MA, USA). U0126 was purchased from MedChemExpress (Monmouth Junction, NJ, USA). Methanol, Hydrochloric Acid, Ethanol, Xylene, Mayer's hematoxylin solution, 1% Eosin Y solution, and PathoMount were purchased from Fujifilm Wako Pure Chemical Industries, Ltd. 9-Aminoacridine (9AA) was purchased from Merck (Darmstadt, Germany). Polyethylene Glycol 600 Sulfate for MALDI-MSI was purchased from Tokyo chemical industry (Tokyo, Japan). Indium tin oxide (ITO)-coated glass slides (100 Ω/sq without adhesive material coating) for MALDI-MSI and adhesive-coated glass slides for hematoxylin and eosin staining (HE), and coverslips were purchased from Matsunami Glass (Osaka, Japan).

The human breast adenocarcinoma MCF-7 cell line was obtained from the American Type Culture Collection (ATCC; Manassas, VA, USA). Cells were grown in Dulbecco's modified Eagle's medium (Nakalai Tesque, Kyoto, Japan) containing 10% (v/v) fetal bovine serum (FBS; Sigma-Aldrich), and antibiotics (100 U/mL penicillin, 100 mg/mL streptomycin, and 0.25 mg/mL amphotericin B; Nakalai Tesque, Kyoto, Japan) at 37 °C under a humidified atmosphere with 5% CO_2.

Quantitative RT-PCR (qRT-PCR) analysis

Real-time PCR analysis was conducted as described previously (*41*). Briefly, RNA was isolated from cells or tissues using NucleoSpin RNA Plus (Macherey-Nagel, Duren, Germany, Cat. No. 740984.250) and subjected to cDNA synthesis using ReverTra Ace qPCR RT Master Mix (TOYOBO, Osaka, Japan) and quantitative PCR using a KOD SYBR qPCR kit (TOYOBO) with CFX96 Real-Time PCR System (Bio-Rad Laboratories, Hercules, CA, USA) according to the manufacturer's protocol. The ΔΔCq method was used to quantify gene expression, using RPL27 or Rplp0 expression as an internal reference (*42*). All experiments were performed in triplicate. The primers used for real-time PCR are listed in Supplementary Table S4.

Western blotting

Immunoblot analysis was performed as described previously (*41*) using primary antibodies against GAPDH (1:2000; Sigma-Aldrich, MAB374), GAPDH (1:4000; Proteintech, MA, USA, 10494-1-AP), αTubulin (1:1000; Abcam, Cambridge, MA, USA, ab15246), IκBα (1:1000; Cell Signaling Technology, Danvers, MA, USA, #4814), IκBα (1:1000; Cell Signaling Technology, #4812), RELA (1:1000; Cell Signaling Technology, #8242), A20 (1:1000; Cell Signaling Technology, #5630), RICTOR (1:500; Santa Cruz Biotechnology, Inc., CA, USA, sc-81538), RICTOR (1:1000; Cell Signaling Technology, #5379), P-RICTOR (1:1000; Cell Signaling Technology, #3806), AKT (1:1000; Cell Signaling Technology, #4685), P-AKT(Ser473) (1:1000; Cell Signaling Technology, #4051), P-AKT(Ser473) (1:1000; Cell Signaling Technology, #4060), P-AKT(Thr308) (1:1000; Cell Signaling Technology, #2965), NT5E (1:1000; Cell Signaling Technology, #13160), HPRT1 (1:1000; 15059-1-AP, Proteintech), HPRT1 (1:500; Santa Cruz Biotechnology, Inc., sc-3769), p21 (1:1000; Cell Signaling Technology, #2947), Cyclin D1 (1:1000; Cell Signaling Technology, #2978), IKKβ (1:1000; Cell Signaling Technology, #2370), P-IKKα/β (Ser176/180) (1:1000; Cell Signaling Technology, #2697), Lamin A (1:1000; Abcam, ab8980), ERK (1:1000; Cell Signaling Technology, #9102), GFP (1:500; Santa Cruz Biotechnology, Inc., sc-5385), and secondary antibodies [HRP-linked anti-mouse IgG (1:5000; Cell Signaling Technology, #7076), HRP-linked anti-goat IgG (1:5000; Santa Cruz Biotechnology, Inc., sc-2020), and HRP-linked anti-rabbit IgG (1:5000; Cell Signaling Technology, #7074)].

For the separation of nuclear fraction, the nuclear and cytoplasmic protein extraction kit (Biovision Inc., Milpitas Boulevard, Milpitas, CA, USA, #K266) was used according to the manufacturer's procedures.

RELA immunocytochemistry

Cells were fixed with 4% paraformaldehyde (Thermo Fisher Scientific) in phosphate buffered saline (PBS) for 15 min, rinsed with PBS, and permeabilized with 0.2% Triton X-100 (Nakalai Tesque) in PBS for 10 min. Cells were blocked using 1% goat serum Thermo Fisher Scientific, #16210–064) in PBS for 15 min and incubated with RELA antibodies (1:1600; Cell Signaling Technology, #8242) diluted in 1% goat serum/PBS at 4 °C overnight. After rinsing in PBS, cells were incubated with Alexa Fluor 488–conjugated secondary antibodies (1:2000; Thermo Fisher Scientific, A32731), 0.125 ng/mL CellMask™ (Thermo Fisher Scientific) as a cell body stain, and 1 μg/mL 4',6-diamidino-2-phenylindole (DAPI; Nacalai Tesque) as a nuclear stain for 1 h at 25 °C in the dark. Fluorescent images were acquired using IN Cell Analyzer 2500HS (Cytiva, Preston, UK) at 20× magnification. Images of 30 fields were taken for each condition. CellProfiler (ver. 3. 1. 9) was used to segment cellular regions from CellMask™ images, to segment nuclear regions from DAPI images, and to quantify RELA signal intensities for each cell (*43*). The nuclear-to-cytoplasm signal ratio for RELA was calculated based on the integrated signal density.

Analysis of cell morphology

Cell morphology analysis was conducted as described previously (*41*). Briefly, Cells were fixed using 4 % paraformaldehyde for 15 min and permeabilized with 0.1 % Triton-X100 for 5 min. Cell membrane and nucleus were stained with 0.125 ng/mL CellMask™ (Thermo Fisher Scientific) and 1 μg/mL DAPI (Nacalai Tesque) for 30 min at 25 °C in the dark, respectively. Fluorescent images were acquired using IN Cell Analyzer 2500HS (Cytiva, Preston, UK) at 20× magnification. CellProfiler (ver. 3. 1. 9) was used to extract geometrical features from the cell images (*43*). DAPI and CellMask™ staining was used to visualize segmentation of the nucleus and cell body, respectively. The following morphological parameters of the cells were evaluated. Area, Form Factor, Solidity, Extent, Orientation, Eccentricity, Compactness, major axis length, minor axis length, maximum ferret diameter, minimum ferret diameter, Perimeter, and Mean radius (total 13 parameters). PCA based on the 13 parameters was performed by the “prcomp” function in the “stats” R package.

Senescence associated β-galactosidase (SA-β-gal) staining

The senescent cells were stained by a senescence β-galactosidase staining Kit (#9860, Cell Signaling Technology), according to the manufacturer’s instructions. Briefly, cells in 12-well plates were washed with PBS, fixed for 10 min in fixative solution, washed

twice with PBS and incubated in SA-β-gal staining solution overnight at 37 °C. Images were acquired with a Keyence BZ-9000 microscope on 20× magnification. Four random views per well were selected to count the number of cells stained positive for SA-β-gal. Each independent experiment was repeated three times and the percentage of SA-β-gal positive cells per field from a total of 12 fields was analyzed with Image J software. DAPI staining was used to identify nuclei and count the number of cells per field. The threshold for identifying senescent cells was set by a positive control (etoposide treatment).

siRNA transfection

siRNA duplexes for *IκBα* (ON-TARGET plus SMART pool, L-004765-00), *RELA* (ON-TARGET plus SMART pool, L-003533-00), *A20* (ON-TARGET plus SMART pool, L-009919-00), *RICTOR* (ON-TARGET plus SMART pool, L-016984-00), *HPRT1* (ON-TARGET plus SMART pool, L-008735-00), and a negative control (D-001810-02) were purchased from Dharmacon/Horizon Discovery (Cambridge, UK). Cells were transfected with siRNA oligomer (final concentration 50 nM) mixed with Lipofectamine RNAiMAX reagent (Thermo Fisher Scientific) in serum-reduced Opti-MEM (Thermo Fisher Scientific) according to the manufacturer's instructions.

Cell-viability assay

Cell viability was measured using trypan blue exclusion assay. 2×10^5 cells/well were seeded in 12-well plates and incubated at 37 °C. After treatment with reagents and/or siRNAs, cells were disaggregated in 400 μL medium and 10 μL of the suspension was mixed with 10 μL trypan blue (Thermo Fisher Scientific). Viable cells were counted using a Countess Automated Cell Counter (Thermo Fisher Scientific).

Cell cycle analysis using the FUCCI biosensor

MCF-7 cells stably expressing the FUCCI biosensor were obtained by the PiggyBac transposase system (*44*). MCF-7 cells were transfected with the pPBbsr2-H2B-iRFP-P2A-mScarlet-I-hGem-P2A-PIP-tag-NLS-mNeonGreen (https://benchling.com/s/seq-LPZ1tLdpgnpJIYOG2ujR) and the hyPBase (https://benchling.com/s/seq-oGkw53b41IZqvzF5yQ9K) (*45*) plasmids using Lipofectamine LTX following manufacturer's protocol (Thermo Fisher Scientific). The plasmids, pPBbsr2-H2B-iRFP-P2A-mScarlet-I-hGem-P2A-PIP-tag-NLS-mNeonGreen and hyPBase, were a gift from Dr. K. Aoki (National Institute for Basic Biology, National Institutes of Natural Sciences). After transfection, cells were released into

drug-free medium for 48 hr followed by blasticidin (10 μg/mL) selection until single colonies were formed. Single clones were expanded, and the FUCCI biosensor signal was confirmed by fluorescent microscopy. Time-lapse microscopy images were acquired using an IN Cell Analyzer 2500HS (GE Healthcare Life Science) with a CFI S Plan Fluor ELWD dry objective lens 20× (NA: 0.45) using an excitation wavelength of 475 nm and emission wavelength of 511 nm for PIP-tag-mNeonGreen and excitation wavelength of 542 nm and emission wavelength of 597nm for mScarlet-hGem. Cells were maintained at 37 °C in a humidified atmosphere of 5% CO_2 and imaged at 20 min intervals for 60 hr. Image processing and quantifications for percentage of cells in each cell cycle phase were performed using tools in ImageJ-Fiji software (version 1.53t, NIH). Masks of mScarlet-hGem and PIP-tag-mNeonGreen signals were obtained by applying a fixed threshold (160, 65535). The obtained masks were identified with 'Analyze Particles' (size = 10.00–infinity, circularity = 0.00–1.00) and automatically counted as ROIs (region of interest). Cell cycle phases were determined by G1-phase: PIP-tag positive, S-phase: hGem positive, G2/M-phase: PIP-tag and hGem positive. The average fluorescence brightness of mScarlet and mNeonGreen was obtained by cell tracking software (Olympus). The threshold parameters of mScarlet and mNeonGreen for each cell were manually set. Then, an algorithm for estimating the cell cycle phase assembled with R packages [brunnermunzel (v.1.4.1), multimode (v.1.4), rlist (v.0.4.6.1), tidyverse (v.1.3.0)] was applied to determine each cell cycle phase at the single-cell level. For quantifications of the G2/M phase length from single-cell data, measurements within 24–60 hr were used when the effects of TNFα were observed.

Generation of IκBα KO MCF-7 cells

IκBα knockout (KO) MCF-7 cells were generated by CRISPR-Cas9 technology. We designed three independent guide RNAs targeting IκBα (*NFKBIA*) with the gRNA design tool (https://chopchop.cbu.uib.no/) (*46*). Two gRNAs were designed to target exon 1 and one gRNA to target intron 1 of *NFKBIA* (Supplementary Table S5). Primers were then designed by adding an additional guanosine base on the 5' and sticky ends corresponding to *BbsI* site. The pair of primers were then annealed and ligated into *BbsI*-digested eCas9-P2A-Puro plasmid (*47*). MCF-7 cells were transfected with IκBα gRNA-containing eCas9-P2A-Puro plasmids using Lipofectamine LTX following manufacturer's protocol (Thermo Fisher Scientific). After transfection, cells were released into drug-free medium for 48 h followed by puromycin (1 μg/mL) selection until single colonies were formed. Single clones were expanded, and gene-deletion was

confirmed by western blotting. eSpCas9(1.1)-T2A-Puro was a gift from Andrea Németh (Addgene, # 101039).

Generation of A20-overexpressing MCF-7 cells

To establish cell lines stably overexpressing A20, the PiggyBac transposase system was used (*44*). The plasmid used for A20 overexpression, pPB[Exp]-EGFP/Puro-CMV>hTNFAIP3, was constructed with VectorBuilder (Kanagawa, Japan). The vector ID is VB220607-1391zue and more information can be obtained from vectorbuilder.com. MCF-7 cells were transfected with the pPB[Exp]-EGFP/Puro-CMV>hTNFAIP3 and hyPBase (*45*) plasmids using Lipofectamine LTX following the manufacturer's protocol. (Thermo Fisher Scientific). After transfection, cells were released into drug-free medium for 48 h followed by puromycin (1 μg/mL) selection until single colonies were formed. Single clones were expanded, and expression of A20 was confirmed by western blotting.

Mouse experiments

All mice were purchased from the Japan SLC and maintained under specific pathogen–free conditions at Graduate School of Frontier Biosciences Osaka University. Female 8-weeks-old (young) and 69–73-weeks-old (aged) C57BL/6 N mice were used in experiments. All animals were separately caged with a 12:12-h light–dark cycle and had free access to water and chow throughout the study. The excised tissues were immediately frozen in liquid nitrogen and stored at −80°C until use. All experiments were approved by the Animal Care and Use Committee of Osaka University and were performed in accordance with institutional guidelines.

Immunohistochemistry of RELA in heart tissue from aged mice

Immunohistochemistry was performed at Genostaff (Tokyo, Japan). Tissue sections were fixed with 4% paraformaldehyde for 10 min. Endogenous peroxidase was blocked with 0.3% H_2O_2 in methanol for 30 min, followed by incubation with G-Block (Genostaff) and avidin/biotin blocking kit (Vector Laboratories, Peterborough, UK). The sections were incubated with anti-REL A rabbit monoclonal antibody (0.004 μg/mL, Cell Signaling Technology, #8242) at 4 □ overnight and then incubated with biotin-conjugated anti-rabbit IgG (Vector Laboratories) for 30 min at room temperature. Subsequently, peroxidase-conjugated streptavidin (Nichirei, Tokyo, Japan) was added for 5 min, and peroxidase activity was visualized using diaminobenzidine. The sections

were counterstained with Mayer's Hematoxylin (Muto Pure Chemicals Co., Ltd., Tokyo, Japan), dehydrated, and then mounted with Malinol (Muto Pure Chemicals Co., Ltd.).

Stained slides were digitally scanned using a NanozoomerS210 (Hamamatsu Photonics, Hamamatsu, Japan). For histopathological assessment, five random digital images of each mouse heart tissue were captured at 40× magnification using NDP view2 software (Hamamatsu Photonics). RELA positive staining in nuclei was quantified by the ImmunotRatio ImageJ plugin (*48*). The brown (RELA) and blue (hematoxylin) threshold adjustments were set at 10 and 15, respectively.

Metabolome analysis

Metabolome analysis was conducted as described previously (*49*). Briefly, the cell samples (approximately 1×10^6 cells), conditioned media (50 L), and heart tissues (approximately 30 mg) were mixed with 1 mL of cold methanol containing 10-camphorsulfonic acid (1.5 nmol) and piperazine-1,4-bis (2-ethanesulfonic acid) (1.5 nmol) as internal standards. Each sample was vigorously mixed by vortexing for 1 min, followed by 5 min of sonication. The extracts were then centrifuged at 16,000 × *g* for 5 min at 4 °C, and the resultant supernatant (400 μL) was collected. Protein concentrations in the pellet were determined using a Pierce™ BCA Protein Assay Kit (Thermo Fisher Scientific, MA). After mixing 400 μL of supernatant with 400 μL of chloroform and 320 μL of water, the aqueous and organic layers were separated by vortexing and subsequent centrifugation at 16,000 × *g* and 4 °C for 5 min. The aqueous (upper) layer (500 μL) was transferred into a clean tube. After the aqueous layer extracts were evaporated under vacuum, the dried extracts were stored at −80 °C until the analysis of hydrophilic metabolites. Prior to analysis, the dried aqueous layer was reconstituted in 50 μL of water.

Two liquid chromatography high-resolution tandem mass spectrometry (LC/MS/MS) methods for hydrophilic metabolite analysis were employed (*49, 50*). Anionic polar metabolites (i.e., organic acids, sugar phosphates, nucleotides, etc.) were analyzed via ionchromatography (Dionex ICS-5000+ HPIC system, Thermo Fisher Scientific) with a Dionex IonPac AS11-HC-4 μm column (2 μm i.d. × 250 mm, 4 μm particle size, Thermo Fisher Scientific) coupled with a Q Exactive high-performance benchtop quadrupole Orbitrap mass spectrometer (Thermo Fisher Scientific) (IC/MS/MS). Cationic polar metabolites (i.e., amino acids, bases, nucleosides, etc.) were analyzed via liquid chromatography (Nexera X2 UHPLC system, Shimadzu) with a Discovery HS F5

column (2.1 mm i.d. × 150 mm, 3 μm particle size, Merck) coupled with a Q Exactive instrument (PFPP-LC/MS/MS). The two analytical platforms for hydrophilic metabolite analysis were controlled using LabSolutions, version 5.80 (Shimadzu) and Xcalibur 4.2.47 (Thermo Fisher Scientific). Metabolome analyses, and data processing were performed at the Division of Metabolomics of the Medical Institute of Bioregulation at Kyushu University. Quantitative levels of metabolites were calculated using peak areas relative to an internal standard (10-camphorsulfonic) and corrected for the total protein amount (analysis for MCF7 cells) or weight (analysis for mouse heart tissues) of each sample.

To interpret the data, the metabolites levels significantly altered by IκBα KD (FDR < 0.05) or aging in the mouse heart (FDR < 0.1) were analyzed for pathway enrichment using the web-based MetaboAnalyst 5.0 software (http://www.metaboanalyst.ca) and KEGG library (http://www.genome.jp/kegg/). Metabolite identifiers (Human Metabolome Database [HMDB] ID, http://www.hmdb.ca) were used for each metabolite.

Analysis for ATP imaging in the mouse heart using MALDI-MSI

Standard sample analysis

To detect ATP, 9AA was used as a matrix. The 9AA was dissolved in distilled water and methanol (3:7, v/v) at a concentration of 5 mg/mL. Each concentration standard solution and matrix solution were equivalent volume mixed. The mixture was spotted on ITO-coated glass slides, dried, and measured.

MALDI-MSI analysis

Frozen serial 8 μm sections of mice heart tissues were cut at −20°C with a Microtome (CM1950; Leica, Nussloch, Germany) and mounted on ITO-coated glass slides for MALDI-MSI and on coated glass slides for HE staining. The sections were dehydrated in a 50 ml conical tube containing silica gel and stored at −80°C.

The prepared matrix solution was applied over 200 μL/section (9AA) with an airbrush (GSI Creos, Tokyo, Japan). After spraying, the samples were immediately measured.

MALDI-MSI experiment was performed on a MALDI ion trap time-of-flight mass spectrometer (iMScope TRIO; Shimadzu, Kyoto, Japan) equipped with a 1-kHz Nd:YAG laser (λ = 355 nm). The laser spot size was approximately 15 μm, and each

pixel was irradiated 80 times at a repetition rate of 1 kHz. For *m/z* calibration, Polyethylene Glycol 600 Sulfate (Tokyo Chemical Industry, Tokyo, Japan) was used. Mass spectra were acquired in the negative ion detection mode. The target m/z values were 505.99 derived from $[M-H]^-$. In the imaging experiment, the interval of data points was 40 µm in the lateral and axial directions. After sample analysis, ion images were reconstructed based on data extracted from *m/z* ranges of the target *m/z* values ± 0.02 Da using Imaging MS solution (Shimadzu, Kyoto, Japan). Signal intensities from region-of-interest were extracted using Imaging MS solution.

Mathematical Model

We constructed the mathematical model of TNFR signaling pathway by extending the previous model (*51*). A comprehensive diagram of the TNFα signaling network is shown in Extended Data Fig. 3a. The mathematical model describes the biochemical reactions using ordinary differential equations, from activation of TNF receptors following transcription of negative feedback regulators (IκBα and A20) by NFκB. The model constitutes 17 ordinary differential equations with 34 parameters and 18 model species. Details about the model equations can be found in Supplementary Table 1–3.

Parameter estimation was performed using BioMASS (ver. 0.7.2) (*52*) (https://github.com/biomass-dev/biomass) by minimizing the sum of cosine similarity between experimental data and simulated values in genetic algorithm (https://ui.adsabs.harvard.edu/abs/2003TJSAI..18..193K/abstract).

The cosine similarity between $\vec{x}_{simulation,i}$ and $\vec{x}_{experiment,i}$, is defined as

$$\mathrm{CS} \equiv \sum_{i=1}^{n}\left(1-\left(\frac{\vec{x}_{simulation,i}\cdot\vec{x}_{experiment,i}}{|\vec{x}_{simulation,i}||\vec{x}_{experiment,i}|}\right)\right),$$

where CS is cosine similarity, $n = 3$ is the number of molecules used in parameter estimation (IKK, IκBα and NFκB), $\vec{x}_{simulation,i}$ is vector for activity of the molecules at each time point in the simulation, $\vec{x}_{experiment,i}$ is vector for activities of the molecule at each experimental time point. $\vec{x}_{simulation,i}\cdot\vec{x}_{experiment,i}$ is the inner product of $\vec{x}_{simulation,i}$ and $\vec{x}_{experiment,i}$, and $|\cdot|$ denotes the magnitude of a vector. A low cosine similarity means that dynamic behaviors of the molecules in simulation are similar to the ones in experiment. We used 30 parameter sets for our model simulation and analysis.

Sensitivity analysis

The sensitivity coefficient of each reaction parameter, S_i, is defined as

$$S_i(q(\boldsymbol{P}), p_i) \equiv \frac{\partial \ln q(\boldsymbol{P})}{\partial \ln p_i} \ ,$$

where p_i is an i-th parameter, $\boldsymbol{P}$ is parameter vector $\boldsymbol{P} = (p_1, p_2, \ldots)$, and $q(\boldsymbol{P})$ is a target function, for example, sum of signals, and oscillatory amplitude and period. The sum of amplitudes of peaks, and average of periods from the first to the second were also used as target functions for the analysis. The sensitivity was calculated by increasing the parameter values by 1%.

RNA-sequencing (RNA-seq) of MCF7 cells and mouse heart tissues

Total RNA was isolated using NucleoSpin RNA Plus (Macherey-Nagel, Duren, Germany, Cat. No. 740984.250). Library construction and RNA□seq were performed using the Illumina sequencing platform (Rhelixa). Poly(A) RNA was prepared with the Poly(A) mRNA Magnetic Isolation Module (New England Biolabs, Ipswich, MA, USA), sequencing library was generated with the NEBNext® Ultra™II Directional RNA Library Prep Kit (New England Biolabs), and paired-end sequencing was processed with the NovaSeq 6000 (Illumina, San Diego, CA).

Acquisition of time course RNA-seq data

Time course bulk RNA-seq data sets (DRA011742 and DRA011743 of DNA Data Bank of Japan) in which gene expression was measured every 15 min after TNFα stimulation in IκBα KD MCF-7 cells were obtained from our previous study (*17*).

MCF-7 RNA-seq data analysis

For analysis of MCF7 RNA-seq, sequencing reads were preprocessed using nf-core/rnaseq pipeline (v.3.5) (*53*) (https://github.com/nf-core/rnaseq/blob/1.4.2/docs/output.md). Read quality was assessed using FastQC (v.0.11.9). Trim Galore (v.0.6.7) was used for adaptor trimming. The resulting reads were mapped onto the GRCh38 genome using STAR (v.2.7.6a) and then quantified by Salmon (v.1.5.2). Protein coding genes registered in GENCODE (https://www.gencodegenes.org/human/release_40.html) were used for downstream analysis. Differentially Expressed Genes (DEGs) were identified using the R package DESeq2 (*54*) by performing a Wald significance test between gene expression levels in

each condition 48 h after TNFα stimulation and calculating adjusted *P*-values and $\log_2$ fold change (TNFα vs IκBαKD+TNFα). Genes with adjusted *P*-value < 0.01 and $\log_2$ fold change > 0.4 were classified as upregulated DEGs, and genes with adjusted *P*-value < 0.01 and $\log_2$ fold change < −0.4 as downregulated DEGs. The expression pattern of each upregulated DEG in Fig. 3a was obtained using time course TPM data. Time course TPM data were Z-scored after the logarithm of 2 was taken before clustering. Clustering was performed using the partitioning around medoids (PAM) algorithm with the R package cluster. Heat maps were created using the R package complexHeatmap (*55*). The creation of the regression line and the calculation of the 95% confidence intervals were calculated by the function "stat_smooth()" of the R package ggplot2 (*56*).

Mouse heart RNA-seq data analysis

Mapping of data to perform Gene/transcript quantification was performed using nf-core/rnaseq pipeline (v3.5.) and the default GRCm38 genome. For TF activity analysis, the DOROTHEA (*57*) Regulon database was used in combination with VIPER (*58*). Only TFs with a confidence score of A and interacting with at least 30 genes were included. Genes that were significantly upregulated with aging were identified using the R package DESeq2 (*54*). Criterion was set as adjusted *P*-values < 0.01 and $\log_2$ fold change > 0.

Assay for transposase-accessible chromatin with high-throughput sequencing (ATAC-seq)

Library preparation, sequencing, and mapping for ATAC-seq were performed at DNAFORM (Yokohama, Japan). Fragmentation and amplification of ATAC-seq libraries were conducted as described previously (*59*). Briefly, approximately 5×10^4 cells were lysed and transposed reactions were carried out using Tn5 Transposase (Illumina, #FC121-1030) at 37 °C for 30 min. The reaction solution was purified with the Qiagen MinElute PCR Purification Kit. PCR with custom Nextera PCR primers was then performed for five cycles using NEBNext Q5 Hot Start HiFi PCR Master Mix (New England Biolabs, Ipswich, MA, USA) (*60*). The number of additional PCR cycles was determined by qPCR of partially amplified products (*60*). The PCR products were purified using Agencourt AMPure XP beads (Beckman Coulter: A63881) by double size selection (left ratio: 1.4x, right ratio: 0.5x) following the manufacturer's protocol. Paired-end sequencing was performed on the Illumina HiSeq sequencer.

MCF7 ATAC-seq data analysis

Mapping and peak call were conducted by ENCODE ATAC-seq pipeline (https://github.com/ENCODE-DCC/atac-seq-pipeline). Reads were mapped to the GRCh38 reference sequence using Bowtie2 (v.2.3.4.3), and duplicate reads were removed with Picard (v.2.20.7) and samtools (v.1.9). Peak calling was performed using MACS2 (v.2.2.4) with default parameters. After removal of blacklist region, consistency of peaks was tested by Irreproducible Discovery Rate (IDR) using IDR (v.2.0.4.2). Peak annotation was conducted by HOMER (v.4.9.1) with default settings. Changes in chromatin accessibility near the transcription start site (TSS ± 5000 bp) per condition in each region and the list of differential accessible peaks that were differentially accessible under IκBα KD+TNFα conditions compared to controls were obtained using DEseq2 (v.1.20.0). The criteria for determining a peak with a difference in accessibility were adjusted *P*-value < 0.05 and $\log_2$ fold change > 0.

RELA chromatin immunoprecipitation-sequencing (ChIP-seq)

ChIP was carried out using the Simple ChIP Enzymatic Chromatin IP Kit (Cell Signaling Technology, #9005) following the manufacturer's protocol. Protein/DNA was crosslinked using 1% formaldehyde. Nuclei were isolated and sheared using an ultrasonicator (Epishear probe sonicator, Active Motif, Carlsbad, CA, USA). The sheared chromatin was incubated with RELA antibody (Abcam, ab7970) and Dynabeads Protein G beads (10004D, Thermo Fisher Scientific). After elution of ChIP products, DNA was purified using MinElute PCR Purification Kit (QIAGEN, 28004), the library was prepared using the TruSeq ChIP Library Preparation Kit (Illumina), and 36-bp single-end sequencing of the libraries was processed with a HiSeq3000 system (Illumina).

RELA ChIP-seq data analysis

Mapping of data to produce BigWig files and call peaks was performed using the nf-core/chipseq pipeline (v.1.2.2) (*53*) (https://doi.org/10.5281/zenodo.3240506) and default GRCh38 genome. BigWig files were quantified by "computeMatrix" and visualized by "plotHeatmap" and "plotPlofile" in deeptools (v3.5.1) (*61*). Each peak was assigned to the TSS of the closest gene by HOMER (v.4.11) (*62*). The RELA target gene was defined as the gene whose peak was within ± 5,000 bp from TSS and They were extracted from each cluster. The number of RELA peaks annotated to each target gene was counted using R.

RELA binding site analysis using public databases

The ChIP Atlas peak browser (*63*) was used to identify RELA binding regions in the mouse genome (mm10). The ChIP-seq peak significance threshold was set to 500 (q value < 1E-50) and ChIP-seq peaks from the groups "TFs and other" and “All cell types” and “RELA” were used. Multiple RELA ChIP peaks in a single region were merged by mergeBed in deeptools (v.3.5.1) (*64*). These RELA ChIP peaks were then assigned to the TSS of the closest gene by HOMER (v.4.11). The final RELA target gene was defined as the gene whose Rela peak was within 500 bp of the TSS. The number of RELA peaks within ±10,000 bp from the TSS annotated to each target gene was then counted on R.

KEGG enrichment analysis

KEGG enrichment was compared by the “comparecluster()” function in clusterProfiler (*65*) R package with “fun = “enrichKEGG”. The result was plotted by the R package “complexHeatmap”. Terms with adjusted *P*-values less than 0.05 were displayed.

Statistics and reproducibility

We performed all experiments at least twice and confirmed similar results. Statistical analyses were performed using GraphPad Prism ver. 8.0 software (GraphPad Software, Inc., La Jolla, CA, USA) and R studio ver. 4.2.2 (Rstudio, Boston, MA, USA). For *in vitro* experiments, data from two or more groups were analyzed using Student’s *t*-tests and one-way analysis of variance (ANOVA), respectively. For *in vivo* experiments, data from two or more groups were analyzed using the Mann–Whitney U and Kruskal–Wallis tests, respectively. Data are represented as mean ± SEM or ± SD; *P* values < 0.05 were considered statistically significant.

Data and materials availability

Metabolome data are included in the Supplementary Data. The sequence data for RNA-seq, ChIP-seq, and ATAC-seq reported in this paper have been deposited in the DNA Data Bank of Japan with accession number DRA015837. Code is available at https://github.com/okadalabipr. All other data will be available upon reasonable request.

References

1. Moiseeva, V. *et al.* Senescence atlas reveals an aged-like inflamed niche that blunts muscle regeneration. *Nature* **613**, 169-178 (2023).
2. López-Otín, C., Blasco, M.A., Partridge, L., Serrano, M. & Kroemer, G. Hallmarks of aging: An expanding universe. *Cell* **186**, 243-278 (2023).

3. Franceschi, C., Garagnani, P., Parini, P., Giuliani, C. & Santoro, A. Inflammaging: a new immune–metabolic viewpoint for age-related diseases. *Nature Reviews Endocrinology* **14**, 576-590 (2018).
4. Childs, B.G., Durik, M., Baker, D.J. & van Deursen, J.M. Cellular senescence in aging and age-related disease: from mechanisms to therapy. *Nat Med* **21**, 1424-1435 (2015).
5. Franceschi, C. & Campisi, J. Chronic inflammation (inflammaging) and its potential contribution to age-associated diseases. *J Gerontol A Biol Sci Med Sci* **69 Suppl 1**, S4-9 (2014).
6. Schafer, M.J. *et al.* The senescence-associated secretome as an indicator of age and medical risk. *JCI insight* **5** (2020).
7. Haga, M. & Okada, M. Systems approaches to investigate the role of NF-κB signaling in aging. *Biochemical Journal* **479**, 161-183 (2022).
8. Bernard, D., Slomianny, C., Vandenbunder, B. & Abbadie, C. cRel induces mitochondrial alterations in correlation with proliferation arrest. *Free Radical Biology and Medicine* **31**, 943-953 (2001).
9. Sfikas, A. *et al.* The canonical NF-κB pathway differentially protects normal and human tumor cells from ROS-induced DNA damage. *Cellular signalling* **24**, 2007-2023 (2012).
10. Taniguchi, K. & Karin, M. NF-κB, inflammation, immunity and cancer: coming of age. *Nature Reviews Immunology* **18**, 309-324 (2018).
11. Mowla, S.N., Perkins, N.D. & Jat, P.S. Friend or foe: emerging role of nuclear factor kappa-light-chain-enhancer of activated B cells in cell senescence. *OncoTargets and therapy* **6**, 1221-1229 (2013).
12. García-García, V.A., Alameda, J.P., Page, A. & Casanova, M.L. Role of NF-κB in Ageing and Age-Related Diseases: Lessons from Genetically Modified Mouse Models. *Cells* **10** (2021).
13. Wibisana, J.N. & Okada, M. Encoding and decoding NF-κB nuclear dynamics. *Curr Opin Cell Biol* **77**, 102103 (2022).
14. Adelaja, A. *et al.* Six distinct NFκB signaling codons convey discrete information to distinguish stimuli and enable appropriate macrophage responses. *Immunity* **54**, 916-930.e917 (2021).
15. Wang, A.G., Son, M., Kenna, E., Thom, N. & Tay, S. NF-κB memory coordinates transcriptional responses to dynamic inflammatory stimuli. *Cell reports* **40**, 111159 (2022).
16. Prescott, J.A., Mitchell, J.P. & Cook, S.J. Inhibitory feedback control of NF-κB

signalling in health and disease. *The Biochemical journal* **478**, 2619-2664 (2021).

17. Ando, M. *et al.* Author Correction: IκBα is required for full transcriptional induction of some NFκB-regulated genes in response to TNF in MCF-7 cells. *NPJ systems biology and applications* **8**, 26 (2022).
18. Cheng, Q.J. *et al.* NF-κB dynamics determine the stimulus specificity of epigenomic reprogramming in macrophages. *Science (New York, N.Y.)* **372**, 1349-1353 (2021).
19. Sen, S., Cheng, Z., Sheu, K.M., Chen, Y.H. & Hoffmann, A. Gene Regulatory Strategies that Decode the Duration of NFκB Dynamics Contribute to LPS-versus TNF-Specific Gene Expression. *Cell Syst* **10**, 169-182.e165 (2020).
20. Wallis, R. *et al.* Senescence-associated morphological profiles (SAMPs): an image-based phenotypic profiling method for evaluating the inter and intra model heterogeneity of senescence. *Aging (Albany NY)* **14**, 4220-4246 (2022).
21. Gorgoulis, V. *et al.* Cellular Senescence: Defining a Path Forward. *Cell* **179**, 813-827 (2019).
22. Werner, S.L. *et al.* Encoding NF-kappaB temporal control in response to TNF: distinct roles for the negative regulators IkappaBalpha and A20. *Genes & development* **22**, 2093-2101 (2008).
23. Ruland, J. Return to homeostasis: downregulation of NF-κB responses. *Nature Immunology* **12**, 709-714 (2011).
24. Ashall, L. *et al.* Pulsatile stimulation determines timing and specificity of NF-kappaB-dependent transcription. *Science (New York, N.Y.)* **324**, 242-246 (2009).
25. Oppelt, A. *et al.* Model-based identification of TNFα-induced IKKβ-mediated and IκBα-mediated regulation of NFκB signal transduction as a tool to quantify the impact of drug-induced liver injury compounds. *NPJ systems biology and applications* **4**, 23 (2018).
26. Huang, Y. *et al.* The hepatic senescence-associated secretory phenotype promotes hepatocarcinogenesis through Bcl3-dependent activation of macrophages. *Cell & Bioscience* **11**, 173 (2021).
27. Nakamura, Y., Iwata, H., Kuwayama, T. & Shirasuna, K. S100A8, which increases with age, induces cellular senescence-like changes in bovine oviduct epithelial cells. *Am J Reprod Immunol* **82**, e13163 (2019).
28. Garcia-Alonso, L., Holland, C.H., Ibrahim, M.M., Turei, D. & Saez-Rodriguez, J. Benchmark and integration of resources for the estimation of human

transcription factor activities. *Genome Res* **29**, 1363-1375 (2019).

29. Oki, S. *et al.* ChIP-Atlas: a data-mining suite powered by full integration of public ChIP-seq data. *EMBO Rep* **19** (2018).
30. Heinz, S. *et al.* Simple combinations of lineage-determining transcription factors prime cis-regulatory elements required for macrophage and B cell identities. *Molecular cell* **38**, 576-589 (2010).
31. Musgrove, E.A., Caldon, C.E., Barraclough, J., Stone, A. & Sutherland, R.L. Cyclin D as a therapeutic target in cancer. *Nature reviews. Cancer* **11**, 558-572 (2011).
32. Szwed, A., Kim, E. & Jacinto, E. Regulation and metabolic functions of mTORC1 and mTORC2. *Physiological reviews* **101**, 1371-1426 (2021).
33. Koedderitzsch, K., Zezina, E., Li, L., Herrmann, M. & Biesemann, N. TNF induces glycolytic shift in fibroblast like synoviocytes via GLUT1 and HIF1A. *Scientific reports* **11**, 19385 (2021).
34. Popa, C., Netea, M.G., van Riel, P.L.C.M., van der Meer, J.W.M. & Stalenhoef, A.F.H. The role of TNF-α in chronic inflammatory conditions, intermediary metabolism, and cardiovascular risk. *Journal of Lipid Research* **48**, 751-762 (2007).
35. Pacitti, A.J., Inoue, Y. & Souba, W.W. Tumor necrosis factor stimulates amino acid transport in plasma membrane vesicles from rat liver. *The Journal of clinical investigation* **91**, 474-483 (1993).
36. DeVito, S., Woodrick, J., Song, L. & Roy, R. Mutagenic potential of hypoxanthine in live human cells. *Mutat Res* **803-805**, 9-16 (2017).
37. Peng, B. *et al.* Defective feedback regulation of NF-kappaB underlies Sjogren's syndrome in mice with mutated kappaB enhancers of the IkappaBalpha promoter. *Proceedings of the National Academy of Sciences of the United States of America* **107**, 15193-15198 (2010).
38. Hasegawa, Y. *et al.* Blockade of the nuclear factor-κB pathway in the endothelium prevents insulin resistance and prolongs life spans. *Circulation* **125**, 1122-1133 (2012).
39. Birder, L.A. *et al.* Purine nucleoside phosphorylase inhibition ameliorates age-associated lower urinary tract dysfunctions. *JCI insight* **5** (2020).
40. Kropotov, A. *et al.* Purine nucleoside phosphorylase controls nicotinamide riboside metabolism in mammalian cells. *Journal of Biological Chemistry*, 102615 (2022).

Acknowledgments

We thank Dr. Keita Iida, Dr. Hiroaki Imoto, Mr. Ken Murakami, and Mr. Masatoshi Haga for discussions regarding computational analysis and critical reading of the manuscript. We also thank Ms. Emiko Suga, Ms. Akimi Mizoguchi, Mr. Hiroki Michida, and Mr. Johannes Nicolaus Wibisana for their help with mouse experiments, qRT-PCR, western blot analysis and plasmid construction. We also thank Dr. Kazuhiro Aoki for the generous gift of the Fucci probe, Mr. Hideya Aragaki from Olympus Corporation for providing the cell tracking software, and Dr. Shigeyuki Magi and Dr. Yutaka Suzuki for their help with the RELA ChIP-seq analysis. We also thank Ms. Maiko Goto and Ms. Nanako Seki for their help with the metabolome analysis. This study was supported by the JSPS KAKENHI (17H06299, M.O.; 17H06302, M.O.; 18H04031, M.O.; JP17H06304; T.B.; JP17H06299, T.B.), the JST CREST Program (JPMJCR21N3, M.O.), the Uehara Memorial Foundation (M.O.), the AMED BINDS Program (JP23ama121055. T.B.), and the Cooperative Research Project Program of the Medical Institute of Bioregulation, Kyushu University (S.T. and T.B.).

Author contributions

Conceptualization: S.T., K. Matsuda, and M.O.; Formal analysis: S.T., K. Matsuda, and K.N.; Funding acquisition: T.B. and M.O.; Investigation: S.T., Y.I., M.T., Y.M., A.I.N., and S.S.; Methodology: S.T., K. Matsuda, K.N., Y.I., M.T., Y.M., A.I.N., S.S., K. Moro, T.B., and M.O.; Project administration: S.T. and M.O.; Resources: K. Moro, T.B., and M.O.; Supervision: K. Moro, T.B., and M.O.; Visualization: S.T., K. Matsuda, K.N., A.I.N., and M.O.; Writing: S.T., K. Matsuda, K.N., A.I.N., and M.O.

Competing interests

The authors have declared that no competing interests exist.

Figure legends

Fig. 1. Effect of NFκB inhibitor alpha (IκBα) knockdown on growth arrest and cellular senescence in MCF-7 cells treated with tumor necrosis factor alpha (TNFα). (**a**) Time-course nuclear nuclear factor κB (NFκB) (RELA) abundance in control and IκBα knockdown (KD) MCF-7 cells treated with TNFα (10 ng/mL) (see the Methods). (**b**) Effect of IκBα KD on cell viability. (**c**) Changes of cell morphology at 24 hr. Scale bars, 100 μm. (**d**) Effect of IκBα KD on SA-β-gal staining. Scale bars, 100 μm. (**e**) Senescence-associated secretory phenotype (SASP) genes expression. (**f**) G2/M ratio (left) and duration (right) in TNFα-treated control and IκBα KD MCF7 cells. (**g**)

Effect of IκBα KD on the protein expression of Cyclin D1. Data represent the mean ± SD [(b), (d), (e), (f, left) and (g)] or ± SE (a), median and interquartile range (25th and 75th percentiles) with error bars showing minimum to maximum (f, right). *P* values were determined using unpaired two-tailed Student's t tests [(b) and (f)] or one-way ANOVA followed by Tukey's test [(c), (d), (e) and (g)]. $^{*}P < 0.05$, $^{**}P < 0.01$.

Fig. 2. Mathematical modeling of NFκB dynamics and the effects of IκBα and A20 knockdown. (**a**, **b,** and **c**) Effect of A20 knockdown (KD) on SA-β-gal staining (a), SASP gene expression (b), and Cyclin D1 protein expression (c) in MCF-7 cells treated with TNFα (10 ng/mL). (**d**) Diagram of the TNFα-NFκB signaling network. (**e**) Simulations of nuclear NFκB abundance in IκBα (upper) and A20 KD (lower) cells treated with TNFα for the indicated time. The color bar indicates the fold change values in IκBα or A20 transcription rate compared to that in the control. (**f**) Time-course nuclear NFκB (RELA) abundance in A20 KD MCF-7 cells treated with TNFα for the indicated time. The control is the same dataset as in Fig. 1a. (**g**) Simulation of nuclear NFκB abundance in IκBα KD cells with 100-fold overexpression (OE) of A20 transcription rate. Black line indicates the simulation of the control cells without A20 OE. Blue lines indicate the simulations of A20 OE cells. The color bar indicates the fold change values in IκBα transcription rate. (**h**) Effect of IκBα KD in time-course nuclear RELA abundance in A20 OE MCF-7 cells. (**i** and **j**) Effect of IκBα KD in SA-β-gal staining (i) and SASP gene expression (j) in MCF-7 cells treated with TNFα. Data represent the mean ± SD [(a), (b), (c), (i) and (j)] or ± SE [(f) and (h)]. *P* values were determined using the one-way ANOVA followed by Tukey's test [(a), (b), (i), and (j)]. *N.S.*, not significant.

Fig. 3. Transcriptional regulation of NFκB *in vitro* and *in vivo*. (**a**) Time-course clustering of mRNA level (Z-scored $\log_2$TPM) in IκBα KD MCF-7 cells stimulated with TNFα (10 ng/mL) up to 150 min. Lines on the right indicate approximate curves; colored areas indicate 95% confidence intervals. (**b**) Effect of IκBα KD on chromatin accessibility for genes in each cluster in MCF-7 cells treated with TNFα (48 hr). Data represent the $\log_2$ fold change (FC) vs. control conditions (**c**) Effect of IκBα KD and TNFα (120 min) on RELA ChIP signal intensity in open chromatin regions. Row in the heatmap indicates the signal intensity in each region. Lines in the line chart shows the average RELA signal intensity. (**d**) Average count of RELA ChIP peaks for NFκB target genes in each cluster. Genes with RELA peaks in the vicinity of TSS were defined as NFκB target genes (4,361 genes). NFκB target genes in each cluster (cluster

1, 19 genes; cluster 2, 75 genes; cluster 3, 24 genes; cluster 4, 54 genes). (**e** and **f**) Protein expression of IκBα (e) and TNFα (f) in the tissues of young (8-weeks-old, N = 8) and aged mice (69–73-weeks-old, N = 8). (**g**) Correlation between the expression FC (IκBα KD+TNFα vs. Control MCF-7) of cluster 2 genes and FC of aged vs. young mice hearts. Cellular senescence-promoting and SASP genes are labeled. (**h**) Average count of RELA ChIP peaks annotated with genes in each group classified based on FC expression in aged mice hearts. (**i**) KEGG enrichment analysis of the high group genes in aged hearts analysis in Extended Data Fig. 7b. Data represent the mean ± SE [(b), (d), and (h)] or median and interquartile range (25th and 75th percentiles) with error bars showing minimum to maximum [(e) and (f)]. *P* values were determined using the Kruskal–Wallis test followed by Steel–Dwass [(b), (d), and (h)] or Mann–Whitney U test [(e) and (f)]. The correlation was analyzed using the Spearman's correlation (g). *N.D.*, not detected.

Fig. 4. Sustained NFκB activation enhances purine catabolism. (**a**) Effect of IκBα KD+TNFα on protein expression of RICTOR and P-RICTOR in MCF-7 cells. (**b**) Volcano plots showing differences in intracellular metabolites in MCF-7 cells under control and IκBα KD+TNFα conditions. (**c**) Intracellular hypoxanthine levels in IκBα KD+TNFα. (**d**) Metabolite pathway enrichment analysis (MPEA) of intracellular metabolite differences between control and IκBα KD+TNFα. (**e**) Schematic purine metabolic pathway. Red indicates upregulation ($P < 0.05$); blue indicates downregulation ($P < 0.05$). (**f**) Effect of IκBα KD on the protein expression of NT5E and HPRT1. (**g**) Effect of HPRT1 KD on SA-β-gal staining. Scale bars, 100 μm. (**h**) Correlation of HPRT and IκBα protein expression in young and aged heart tissues. (**i**) MPEA for the differential metabolites between heart tissues of young and aged mice. (**j**) Metabolites significantly changed in the purine metabolic pathway between young and aged heart tissues. Young mice: 8-weeks-old, N = 8. Aged mice: 69–73-weeks-old, N = 8. (**k**) Mass spectrometric images of ATP levels in young and aged heart tissues. The percentage shows the ATP level relative to young heart #1. Upper, young hearts; lower, aged hearts. Data represent the mean ± SD [(a), (c), (f), (g) and (j)]. *P* values were determined using unpaired two-tailed Student's t tests (e), one-way ANOVA followed by Tukey's test [(a), (c), (f), and (g)], or Mann–Whitney U test (j). The correlation was analyzed using the Spearman's correlation (h). $^{*}P < 0.05$, $^{**}P < 0.01$, $^{***}P < 0.001$.

Extended Data Fig. 1. Effect of IκBα knockdown/knockout on cellular senescence. (**a**) IκBα knockdown in MCF-7 cells by siRNA. MCF-7 cells were treated with TNFα

(10 or 30 ng/mL) for 24 or 48 hr. Representative blot images. The values under each lane indicated relative density of the band normalized to GAPDH. (**b**) Representative images of RELA immunofluorescence staining in the MCF-7 cells transfected with control and *IκBα* siRNA. The cells were treated with 10 ng/mL TNFα for the indicated times. Scale bars, 25 μm. (**c**) Principal component analysis of 13 geometric parameters for single cells (**d**) Changes of the geometric parameters for single cells. *P* values were determined using one-way ANOVA followed by Tukey's test. (**e**) IκBα knockout (KO) in MCF-7 cells by CRISPR-Cas9. Left: Representative blot images. Right: Bar plots showing quantification of relative protein level of IκBα. (**f**) Effect of IκBα KO on cell viability in MCF-7 cells treated with TNFα (10 ng/mL) for 48 hr. (**g**) Effect of IκBα KO on SA-β-gal staining in MCF-7 cells. Data represent the mean ± SD [(e), (f), and (g)]. *P* values were determined using one-way ANOVA followed by Tukey's test [(d), (f) and (g)].

Extended Data Fig. 2. Effect of IκBα knockdown on SASP expression and cell cycle (**a** and **b**) Knockdowns of RELA and IκBα in MCF-7 cells by siRNAs. MCF-7 cells were treated with TNFα (10 ng/mL) for 48 hr. Representative blot image (a). Bar plots showing quantification of relative protein level of RELA and IκBα (b). (**c**) Effect of RELA KD on the IκBα KD-induced SA-β-gal staining. Representative images. Scale bars, 100 μm. *N.S.*, not significant. (**d**) Heatmap of mRNA expression of SASP genes in MCF-7 cells under IκBα KD+TNFα conditions. The mRNA level of SASP genes was measured by RNA-seq. (**e** and **f**) Cell cycle analysis of MCF-7 cells under IκBα KD+TNFα conditions**.** MCF-7 cells transfected with the control and IκBα siRNA and treated with 10 ng/mL TNFα for the indicated times. (e) Representative images of FUCCI immunofluorescence. MCF-7 cells show G1-phase (green color; PIP-tag-mNeonGreen), S-phase (magenta color; mScarlet-hGem) and G2/M-phase (merged color; PIP-tag-mNeonGreen and mScarlet-hGem) Scale bars, 100 μm. (f) Cell cycle dynamics mapped at an individual cell level (N = 24). Cell cycle phase data were obtained for cells that could be continuously tracked for 60 hr after TNFα treatment. Since the experiment was performed under non-synchronized cell cycle conditions, an equal number of cells starting from the G1 or S/G2/M phase (N = 12 for each) were selected for analysis. (**g**) Effect of A20 knockdown (KD) on protein expression of A20 and Cyclin D1 in MCF-7 cells. Representative blot images. Asterisk indicates a non-specific band. (**h**) Effect of A20 KD on SA-β-gal staining in MCF-7 cells treated with TNFα (10 ng/mL). Representative images. Scale bars, 100 μm. Data represent the

mean ± SD [(b) and (c)]. *P* values were determined using one-way ANOVA followed by Tukey's test (c).

Extended Data Fig. 3. Experimental data used for model training. (**a**) Detailed diagram of the TNFα signaling network. Each box represents a regulatory module leading from the IKK-IκBα-NFκB module to the transcription and translation module. Black arrows represent biochemical modifications, association/dissociation, and transport of proteins. Red numbers indicate model reaction indices. (**b**) Protein expression of nuclear RELA in MCF-7 cells treated with TNFα (10 ng/mL) for the indicated time (upper panel). Protein expression of P-IKKα/β, IKKβ, and IκBα in MCF-7 cells treated with TNFα for the indicated time (lower panel). (**c**) Time-course patterns of P-IKK, total IκBα, and total nuclear NFκB in MCF-7 cells treated with TNFα (10 ng/mL) for the indicated time (upper). Results of model predictions (*IκBα* and *A20* mRNA) (lower). Circles represent experimental data (the mean ± SD, N = 3) and lines represent the averaged trajectories of 30 simulation runs. The darker colored line represents the average of the simulation results using 30 independently searched parameter sets. The lighter colored lines represent the simulation results for the individual parameter sets. (**d**) Estimated 30 parameter sets. The box plot shows the range of values for 30 parameter sets estimated from the time-course experimental datasets shown in Extended Data Fig. 3c. The horizontal axis shows the indices of the estimated model parameters. The vertical axis shows the parameter values and protein abundances (TTR, IKK and IκBα-NFκB).

Extended Data Fig. 4. Model simulation of NFκB dynamics under conditions of knockdown or overexpression of IκBα or A20. (**a** and **b**) Simulations of nuclear NFκB dynamics in IκBα (a) or A20 (b) downregulation in response to TNFα. Each line is presented as the mean of simulation values for 30 parameter sets. The color bar indicates the fold change values in IκBα or A20 transcription rate compared to that in the control. The data were normalized between minimum (0) and maximum (1) values in control. (**c** and **d**) Simulations of nuclear NFκB dynamics in IκBα (c) or A20 (d) overexpression in response to TNFα. (**e**) Sensitivity analysis against nuclear NFκB activity. Nuclear NFκB activity was defined as the area under the curve (AUC), which is the sum of NFκB signals (left). Sensitivity of each parameter to nuclear NFκB activity (right). Lager changes in the graph indicates larger sensitivities against the 1% change in reaction parameters in the model diagram in Extended Data Fig. 3a. Error bars indicate mean ± SD of the 30 parameter sets.

Extended Data Fig. 5. Effect of downregulation or overexpression of A20 on NFκB nuclear dynamics. (**a**) Representative images of RELA immunofluorescence staining in the MCF-7 cells transfected with the control and *A20* siRNA. The cells were treated with 10 ng/mL TNFα for the indicated times. Scale bars, 25 μm. The control is same dataset used in Fig 1a. (**b**) Model simulation of NFκB dynamics in IκBα KD and A20 overexpression conditions. Simulations of nuclear NFκB dynamics in IκBα KD and A20 overexpression in response to TNFα. Each line is presented as the mean of simulation values for 30 parameter sets. The color bar indicates the fold change values in IκBα transcription rate compared to that in the control. The data were normalized between minimum (0) and maximum (1) values in control. (**c**) Overexpression of A20 in MCF-7 cells. Representative blot image of A20 and EGFP protein. Asterisks indicate a non-specific band. (**d**) Effect of IκBα downregulation on NFκB nuclear dynamics in A20-overexpressing MCF-7 cells. Representative images of RELA immunofluorescence staining in parent MCF7-cells and A20-overexpressing MCF-7 cells transfected with the control and *IκBα* siRNA. The cells were treated with 10 ng/mL TNFα for the indicated times. Scale bars, 25 μm.

Extended Data Fig. 6. Differentially expressed genes (DEGs) and proteins in MCF-7 cells and mice. (**a**) Volcano plot of differentially expressed genes (DEGs) between TNFα alone and IκBα KD+ TNFα in MCF-7 cells. Red dots indicate DEGs identified by adjusted *P* value (padj) < 0.01 and $\log_2$ fold change ($\log_2$ FC) > 0.4. Blue dots indicate DEGs identified by padj < 0.01 and $\log_2$ FC < -0.4. Among the DEGs, the cellular senescence-promoting and SASP genes are labeled. (**b**) MA plot of control vs IκBα KD+TNFα ATAC-seq signals. Each dot represents each open chromatin region, red dots indicate open chromatin regions identified by padj < 0.05 and $\log_2$ FC > 0. (**c**) Heatmap of KEGG enrichment analysis of each cluster genes identified in Fig. 3A. (**d** and **e**) Expression of IκBα, A20, and TNFα in young and aged mice tissues. Protein expression of IκBα, A20, and TNFα in young and aged mice tissues. Young mice: 8-weeks-old, N = 8. Aged mice: 69–73-weeks-old, N = 8. Representative blot images (d). Box plots showing quantification of the relative protein level of A20 (e). Data represent the median and interquartile range (25th and 75th percentiles) with error bars showing minimum to maximum. *P* values were determined using the Mann–Whitney U test (e).

Extended Data Fig. 7. Sustained NFκB activity induces higher expression of genes with higher RELA peak numbers in mice hearts. (**a**) Bar plot of transcription factor activity predicted by DorothEA. Confidence was set to A, minsize to 30. (**b**) Venn diagram of NFκB target genes. Light blue circle indicates NFκB target genes and pink circle indicates genes whose expression is markedly upregulated in aged mice (padj < 0.01, FC > 0). Genes included in the pink circle were classified according to the degree of gene expression with aging. (Low: 0 < FC ≤ 0.5, Medium: 0.5 < FC ≤ 1.0, High: 1.0 < FC). (**c**) Immunohistochemistry of RELA in heart tissues from young and aged mice. Young mice: 8-weeks-old, N = 3. Aged mice: 69–73-weeks-old, N = 3. Left: representative images. Scale bars, 50 μm. Right: bar plots showing the percentage of RELA positive staining relative to nuclear area. Five HPFs were obtained from each heart tissue. Data represent the mean ± SD per HPF. *P* values were determined using the Mann–Whitney U test (c).

Extended Data Fig. 8. Effect of sustained NFκB activation in mTORC2 signaling. (**a** and **b**) Effect of AKT inhibitor on Cyclin D1 expression in MCF-7 cells under IκBα+ TNFα conditions. Expression of CyclinD1 in IκBα KD MCF-7 cells treated with TNFα and inhibitor. Representative blot images (a). Bar plots showing quantification of relative Cyclin D1 level in each inhibitor condition (b). Cells were treated with BAY11-7085 (5 μM, NFκB inhibitor), AKTi VIII (1 μM, AKT1/2 inhibitor), LY294002 (10 μM, PI3K inhibitor), Rapamycin (100 nM, mTOR inhibitor), U01268 (10 μM, MEK inhibitor), SB216763 (10 μM, GSK3β inhibitor), SB203580 (10 μM, inhibitor for p38 and AKT), and TNFα for 48 hr. MG132 (10 μM, proteosome inhibitor) was added 8 hr before collecting samples. (**c**) Expression of the mTORC2 pathway proteins in IκBα KD MCF-7 cells treated with TNFα for 48 hr. Representative blot image. Asterisk indicates a non-specific band. (**d**) Effect of RICTOR knockdown (KD) on SA-β-gal staining in MCF-7 cells. Right; representative images. Scale bars, 100 μm. Left; Bar plots showing the percentage of SA-β-gal positive cells. Data represent the mean ± SD. (**e**) Effect of RICTOR KD on Cyclin D1 expression. Left; Representative blot image. Right; Bar plots showing quantification of relative protein levels of RICTRO and HPRT1. The cells were treated with TNFα (10 ng/mL) for 48 hr. Data represent the mean ± SD. (**f**) Effect of AKT inhibitor VIII (10 μM) on SA-β-gal staining and cell viability in IκBα KD MCF-7 cells treated with TNFα. SA-β-gal staining in IκBα KD MCF-7 cells treated with TNFα and AKT inhibitor VIII (10 μM) for 24 hr. Data represent the mean ± SD. [(d), (e), and (f)]. *P* values were determined using the

unpaired one-way ANOVA followed by using one-way ANOVA followed by Tukey's test [(d), (e), and (f)]. *N.S.*, not significant.

Extended Data Fig. 9. Effect of sustained NFκB activation on purine metabolism in MCF-7 cells. (**a**) Principal component analysis of metabolome data (intracellular) of IκBα KD MCF-7 cells treated with TNFα for 48 hr. (**b**) Volcano plots showing differences in extracellular metabolites in MCF-7 cells under control and IκBα KD conditions. (**c**) Extracellular hypoxanthine levels in IκBα KD MCF-7 cells treated with TNFα. (**d**) Effect of IκBα knockdown (KD) on the mRNA expression of purine metabolism genes in MCF-7 cells. The cells were treated with TNFα (10 ng/mL) for 48h. (**e**) Effect of NT5E inhibitor APCP on SA-β-gal staining in IκBα KD MCF-7 cells treated with TNFα. Upper; Representative images. Scale bars, 100 μm. Lower; Bar plot indicating the percentage of SA-β-gal positive cells. (**f**) HPRT1 knockdown in MCF-7 cells by siRNA. Left; Representative blot image. Right; Bar plots showing quantification of the relative protein level of HPRT1. Data represent the mean ± SD. (**g**) Effect of RICTOR knockdown on protein expression of NT5E and HPRT1 in MCF-7 cells. Left; Representative blot image. Right; Bar plots showing quantification of relative protein level of NT5E and HPRT1. Data represent the mean ± SD [(c), (d), (e), (f), and (g)]. *P* values were determined using one-way ANOVA followed by Tukey's test [(c), (d), (e), and (g)]. $^{*}P < 0.05$, $^{**}P < 0.01$, $^{***}P < 0.001$.

Extended Data Fig. 10. Protein expression of RICTOR, RICTOR, and HPRT1 in young and aged hearts. (**a** and **b**) Protein expression of RICTOR, P-RICTOR, and HPRT in young and aged mice tissues. Young mice: 8-weeks-old, N = 8. Aged mice: 69–73-weeks-old, N = 8. Representative blot images (a). Box plots showing quantification of the relative protein level of A20 (b). Data represent the median and interquartile range (25th and 75th percentiles) with error bars showing minimum to maximum. *P* values were determined using the Mann–Whitney U test. (**c**) Mass spectrum of mouse heart. A negative ion mode (*m/z* 340 to *m/z* 530) mass spectrum of mouse heart tissues. The asterisk indicates peak of ATP. (**d**) Effect of H_2O_2 on IκBα protein expression in MCF-7 cells. MCF-7 cells were treated with H_2O_2 for 96 hr. The values under each lane indicated relative density of the band normalized to ERK.

Fig. 1

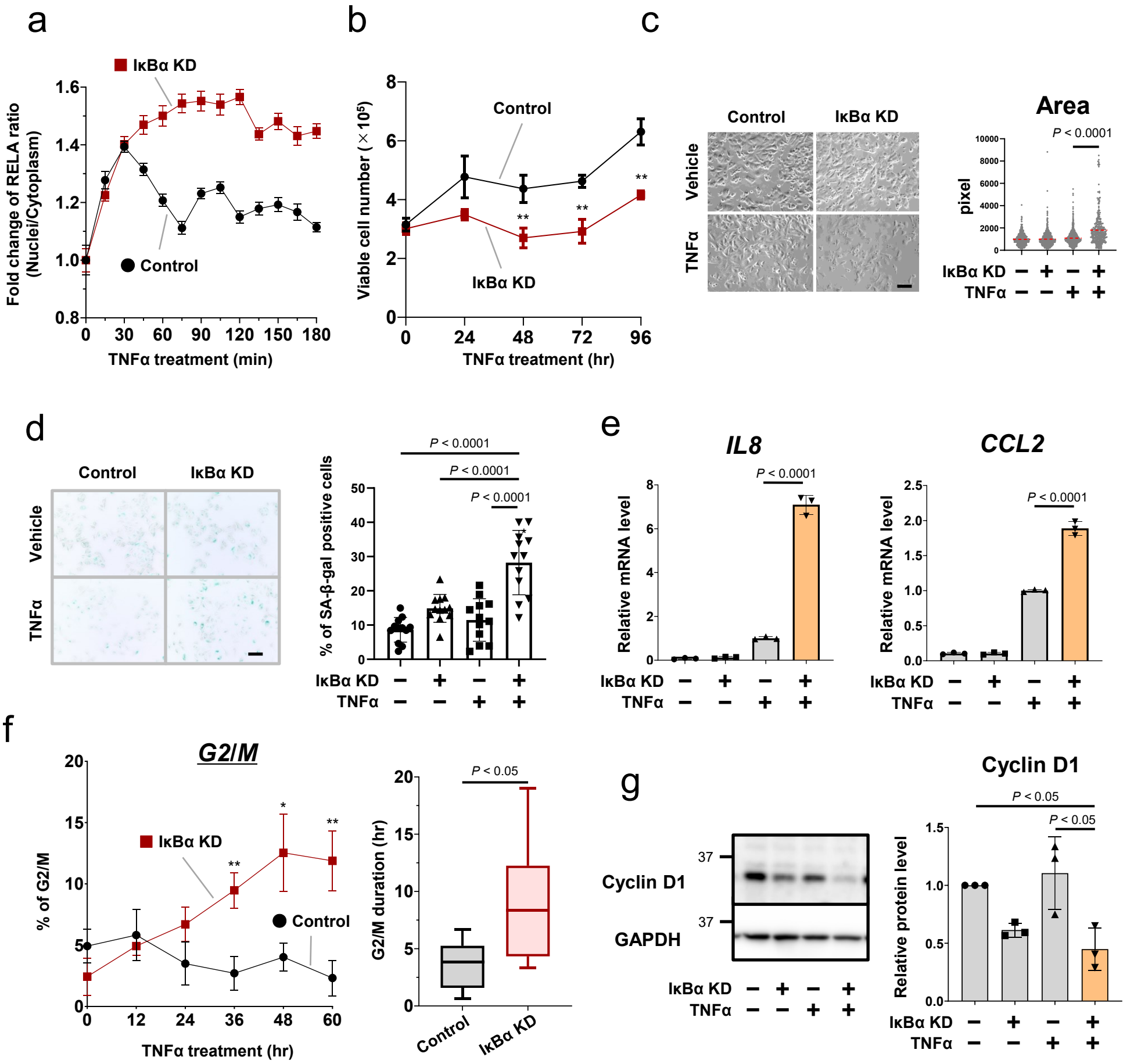
a
IκBα KD
Control
Fold change of RELA ratio (Nuclei/Cytoplasm)
TNFα treatment (min)
b
Control
IκBα KD
Viable cell number (×10⁵)
TNFα treatment (hr)
c
Control
IκBα KD
Vehicle
TNFα
Area
P < 0.0001
pixel
IκBα KD
TNFα
d
Control
IκBα KD
Vehicle
TNFα
P < 0.0001
% of SA-β-gal positive cells
IκBα KD
TNFα
e
IL8
CCL2
P < 0.0001
Relative mRNA level
IκBα KD
TNFα
f
G2/M
IκBα KD
Control
% of G2/M
TNFα treatment (hr)
P < 0.05
G2/M duration (hr)
Control
IκBα KD
g
Cyclin D1
GAPDH
37
IκBα KD
TNFα
Cyclin D1
P < 0.05
Relative protein level
IκBα KD
TNFα

Fig. 2

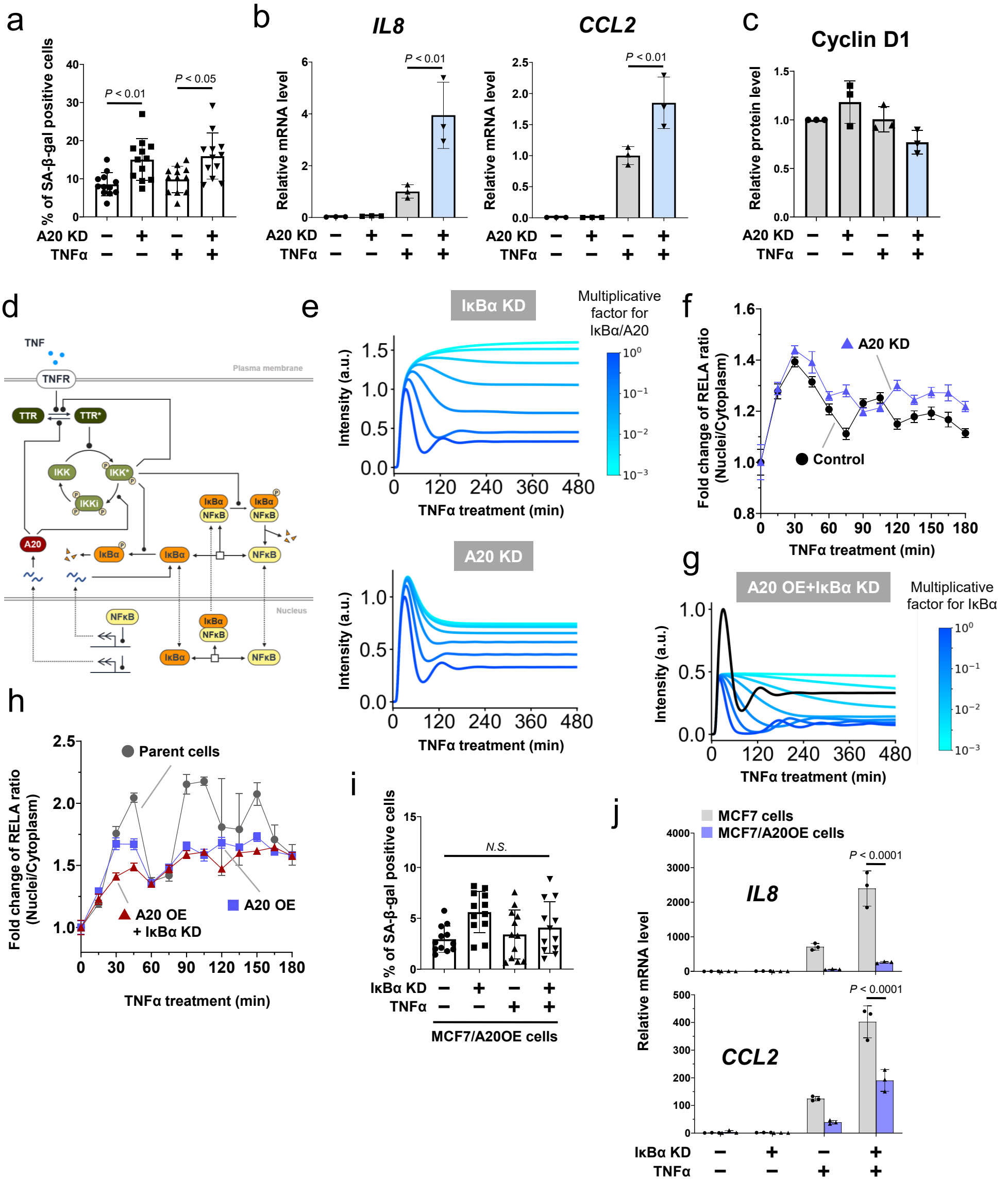
a
% of SA-β-gal positive cells
P < 0.01
P < 0.05
A20 KD
TNFα
b
IL8
CCL2
Relative mRNA level
P < 0.01
c
Cyclin D1
Relative protein level
d
TNF
TNFR
Plasma membrane
TTR
TTR*
IKK
IKK*
IKKi
A20
IκBα
NFκB
Nucleus
e
IκBα KD
Multiplicative factor for IκBα/A20
Intensity (a.u.)
TNFα treatment (min)
A20 KD
f
Fold change of RELA ratio (Nuclei/Cytoplasm)
A20 KD
Control
TNFα treatment (min)
g
A20 OE+IκBα KD
Multiplicative factor for IκBα
Intensity (a.u.)
TNFα treatment (min)
h
Parent cells
A20 OE
A20 OE + IκBα KD
Fold change of RELA ratio (Nuclei/Cytoplasm)
TNFα treatment (min)
i
% of SA-β-gal positive cells
N.S.
IκBα KD
TNFα
MCF7/A20OE cells
j
MCF7 cells
MCF7/A20OE cells
IL8
CCL2
P < 0.0001
Relative mRNA level
IκBα KD
TNFα

Fig. 3

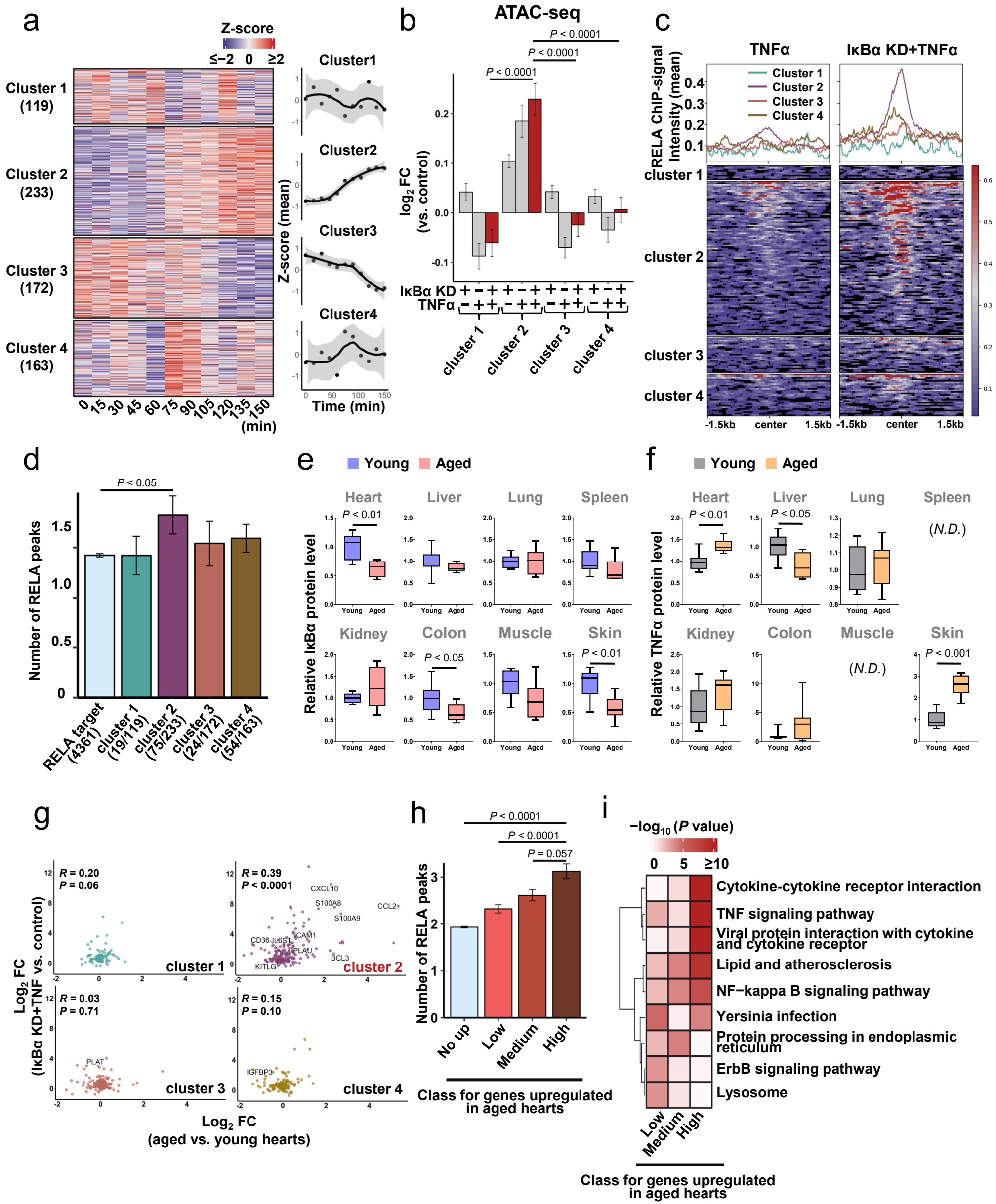
a
Z-score
≤−2 0 ≥2
Cluster 1 (119)
Cluster 2 (233)
Cluster 3 (172)
Cluster 4 (163)
0 15 30 45 60 75 90 105 120 135 150 (min)
Cluster1
Cluster2
Cluster3
Cluster4
Z-score (mean)
Time (min)
b
ATAC-seq
P < 0.0001
P < 0.0001
P < 0.0001
log2 FC (vs. control)
IκBα KD
TNFα
cluster 1
cluster 2
cluster 3
cluster 4
c
TNFα
IκBα KD+TNFα
RELA ChIP-signal Intensity (mean)
Cluster 1
Cluster 2
Cluster 3
Cluster 4
cluster 1
cluster 2
cluster 3
cluster 4
-1.5kb center 1.5kb
d
P < 0.05
Number of RELA peaks
RELA target (4361)
cluster 1 (19/119)
cluster 2 (75/233)
cluster 3 (24/172)
cluster 4 (54/163)
e
Young Aged
Heart
Liver
Lung
Spleen
Kidney
Colon
Muscle
Skin
P < 0.01
P < 0.05
P < 0.01
Relative IκBα protein level
f
Young Aged
Heart
Liver
Lung
Spleen
Kidney
Colon
Muscle
Skin
P < 0.01
P < 0.05
(N.D.)
P < 0.05
(N.D.)
P < 0.001
Relative TNFα protein level
g
R = 0.20
P = 0.06
cluster 1
R = 0.39
P < 0.0001
CXCL10
S100A8
CCL2
S100A9
ICAM1
CD36
IL6ST
PLAU
BCL3
KITLG
cluster 2
R = 0.03
P = 0.71
PLAT
cluster 3
R = 0.15
P = 0.10
IGFBP3
cluster 4
Log2 FC (IκBα KD+TNF vs. control)
Log2 FC (aged vs. young hearts)
h
P < 0.0001
P < 0.0001
P = 0.057
Number of RELA peaks
No up
Low
Medium
High
Class for genes upregulated in aged hearts
i
−log10 (P value)
0 5 ≥10
Cytokine-cytokine receptor interaction
TNF signaling pathway
Viral protein interaction with cytokine and cytokine receptor
Lipid and atherosclerosis
NF−kappa B signaling pathway
Yersinia infection
Protein processing in endoplasmic reticulum
ErbB signaling pathway
Lysosome
Low
Medium
High
Class for genes upregulated in aged hearts

Fig. 4

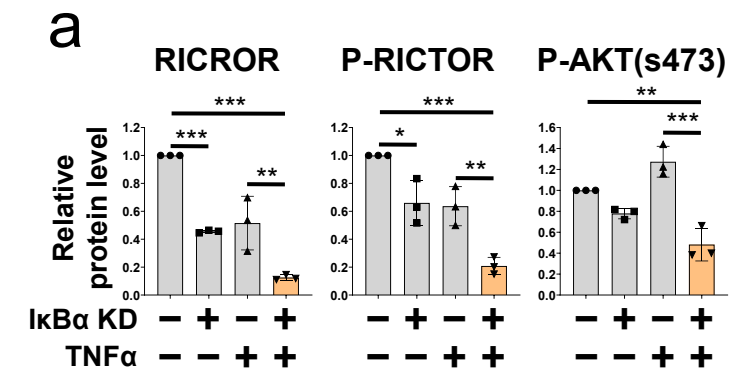
a
RICROR
P-RICTOR
P-AKT(s473)
Relative protein level
IκBα KD
TNFα

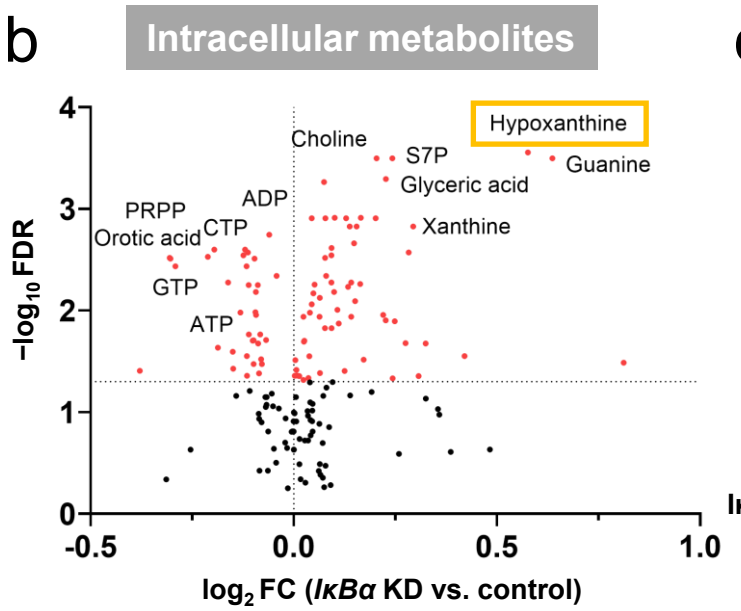
b
Intracellular metabolites
Hypoxanthine
Choline
S7P
Guanine
Glyceric acid
ADP
PRPP
Orotic acid
CTP
Xanthine
GTP
ATP
−log10 FDR
log2 FC (IκBα KD vs. control)

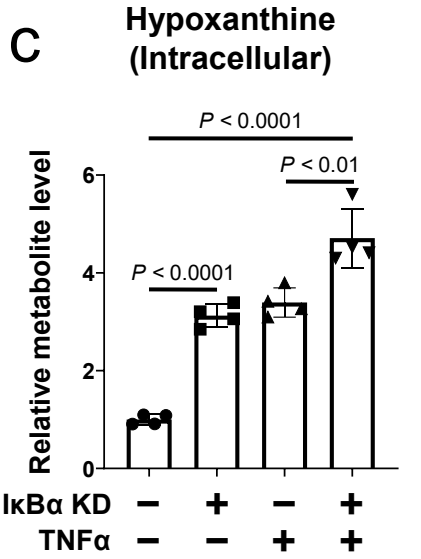
c
Hypoxanthine (Intracellular)
P < 0.0001
P < 0.01
P < 0.0001
Relative metabolite level
IκBα KD
TNFα

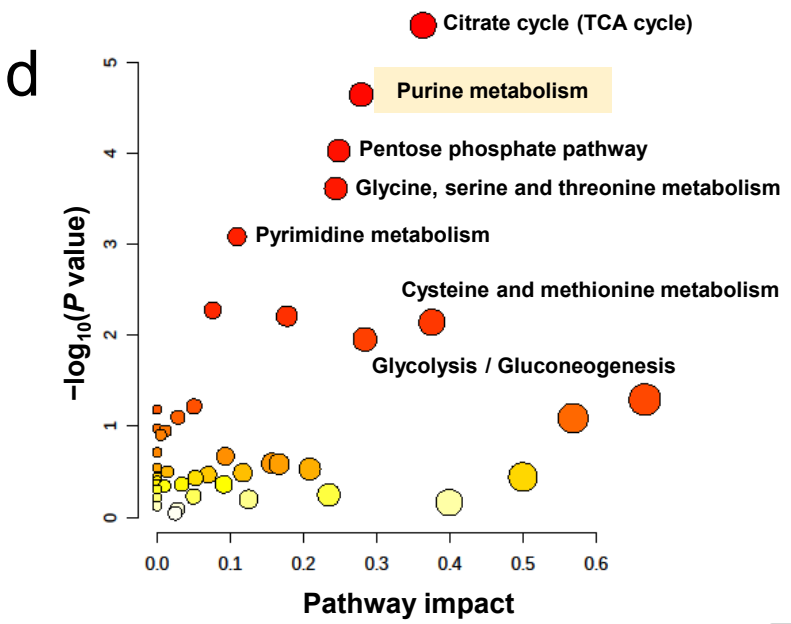
d
Citrate cycle (TCA cycle)
Purine metabolism
Pentose phosphate pathway
Glycine, serine and threonine metabolism
Pyrimidine metabolism
Cysteine and methionine metabolism
Glycolysis / Gluconeogenesis
−log10(P value)
Pathway impact

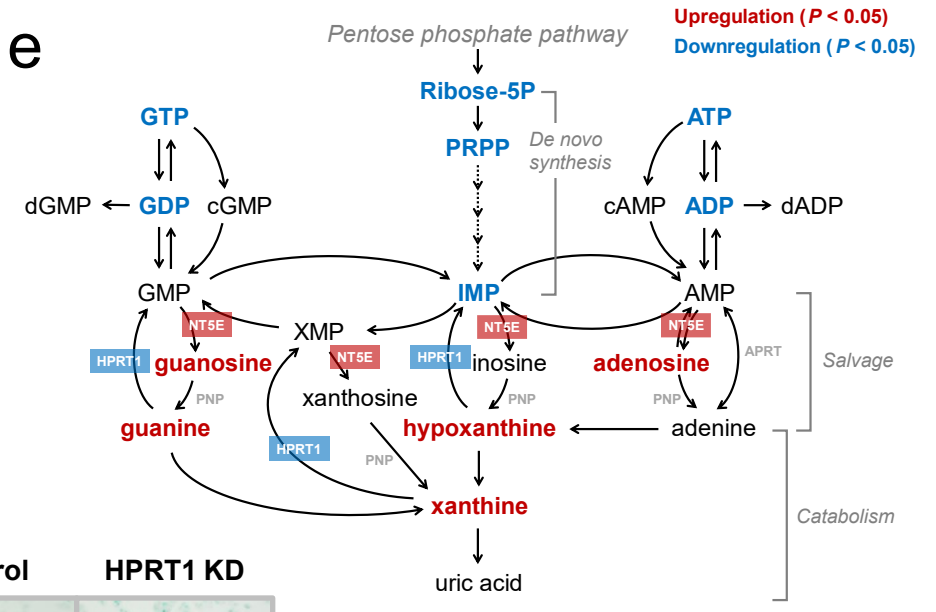
e
Upregulation (P < 0.05)
Downregulation (P < 0.05)
Pentose phosphate pathway
Ribose-5P
PRPP
De novo synthesis
GTP
ATP
dGMP
GDP
cGMP
cAMP
ADP
dADP
GMP
IMP
AMP
XMP
NT5E
HPRT1
guanosine
inosine
adenosine
xanthosine
guanine
hypoxanthine
adenine
PNP
APRT
Salvage
xanthine
Catabolism
uric acid

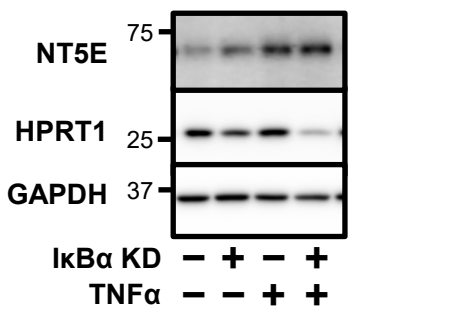
f
NT5E
HPRT1
GAPDH
75
25
37
IκBα KD
TNFα

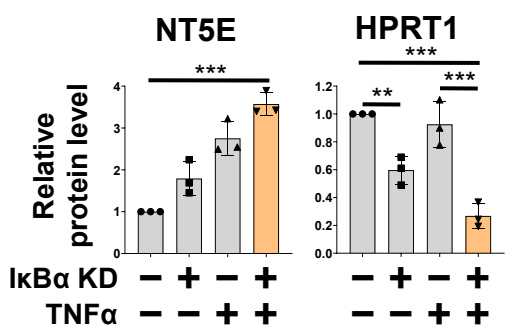
NT5E
HPRT1
Relative protein level
IκBα KD
TNFα

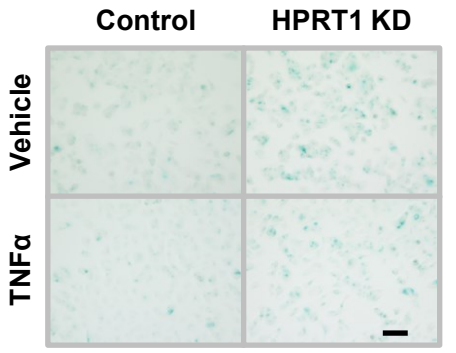
g
Control
HPRT1 KD
Vehicle
TNFα

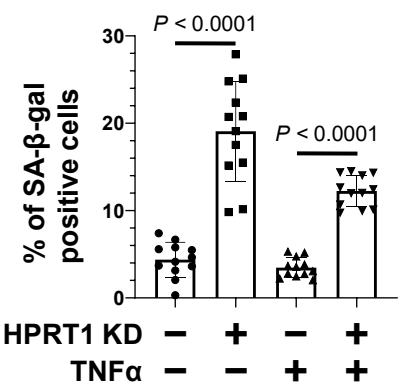
P < 0.0001
P < 0.0001
% of SA-β-gal positive cells
HPRT1 KD
TNFα

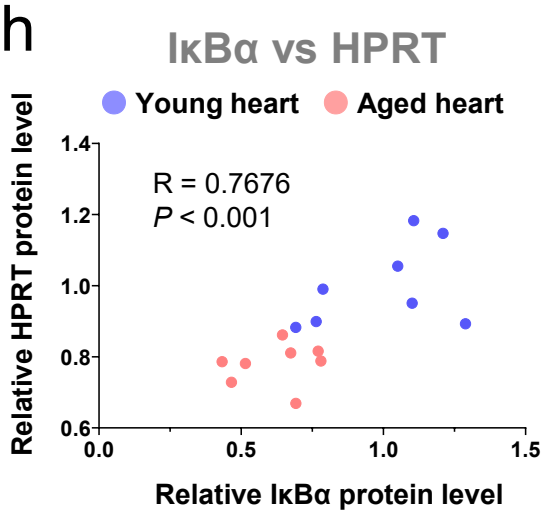
h
IκBα vs HPRT
Young heart
Aged heart
R = 0.7676
P < 0.001
Relative HPRT protein level
Relative IκBα protein level

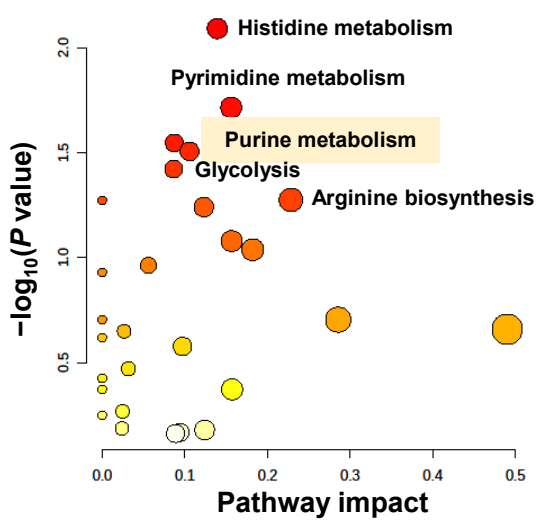
i
Histidine metabolism
Pyrimidine metabolism
Purine metabolism
Glycolysis
Arginine biosynthesis
−log10(P value)
Pathway impact

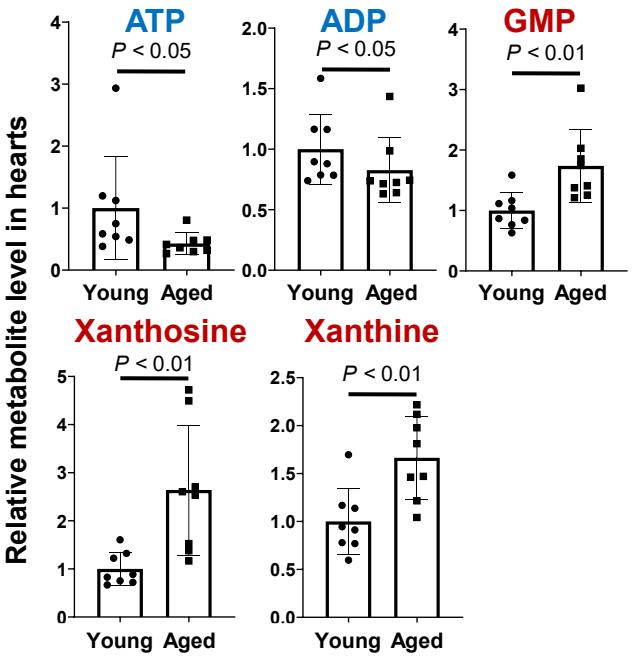
j
ATP
P < 0.05
ADP
P < 0.05
GMP
P < 0.01
Xanthosine
P < 0.01
Xanthine
P < 0.01
Young
Aged
Relative metabolite level in hearts

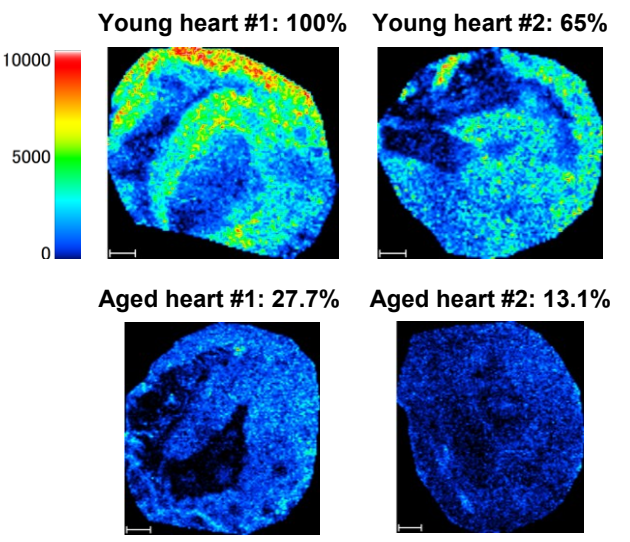
k
Imaging of ATP
Young heart #1: 100%
Young heart #2: 65%
Aged heart #1: 27.7%
Aged heart #2: 13.1%
10000
5000
0

Extended Data Fig. 1

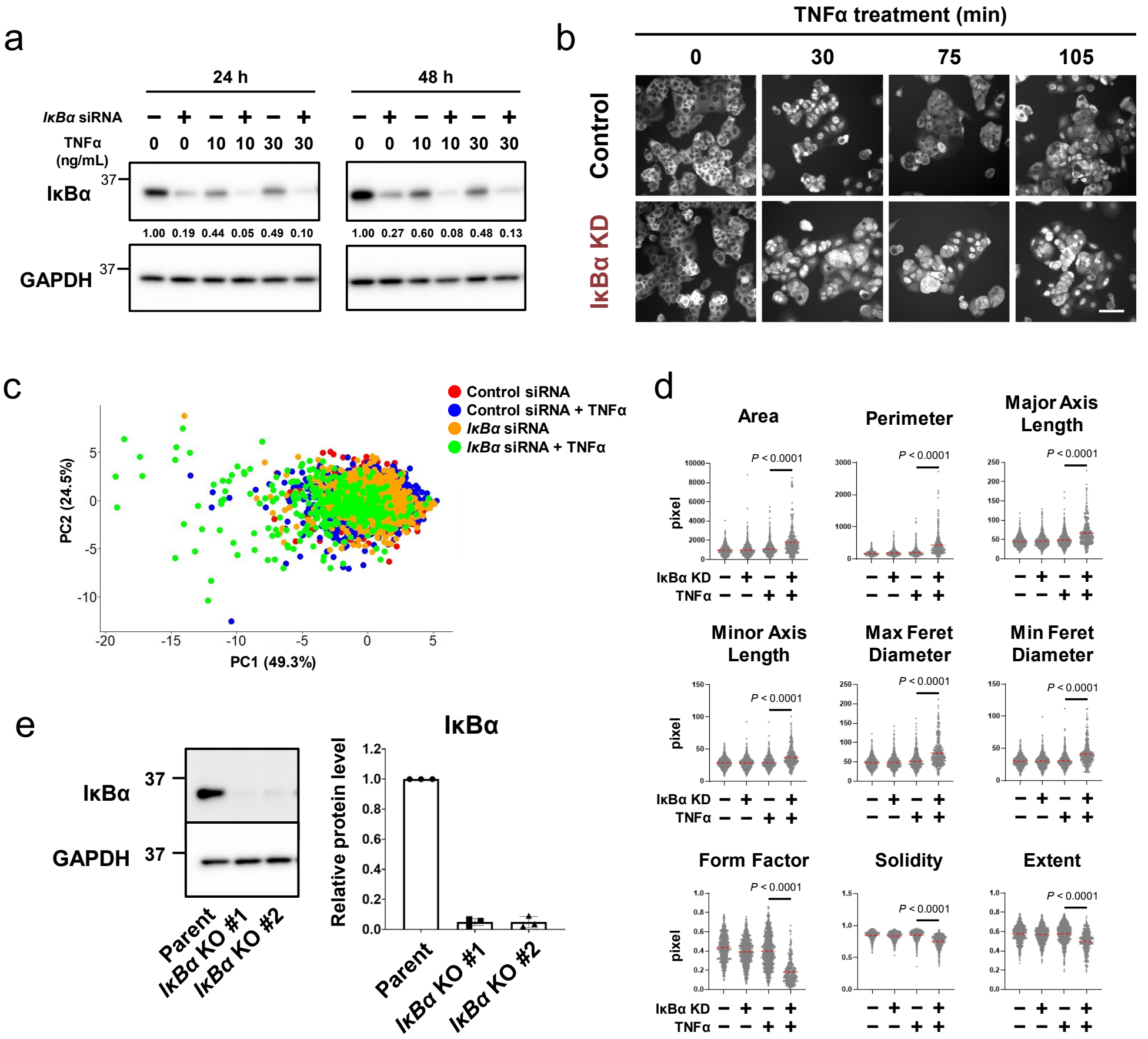

Extended Data Fig. 2

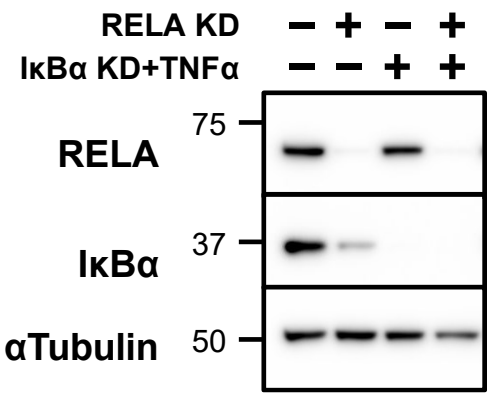

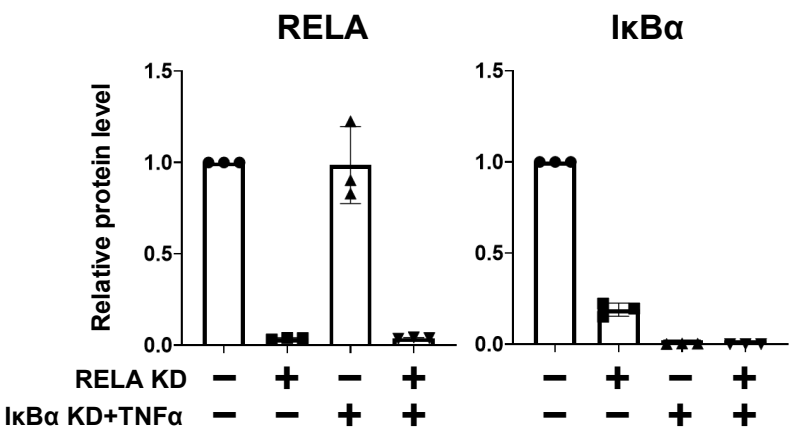

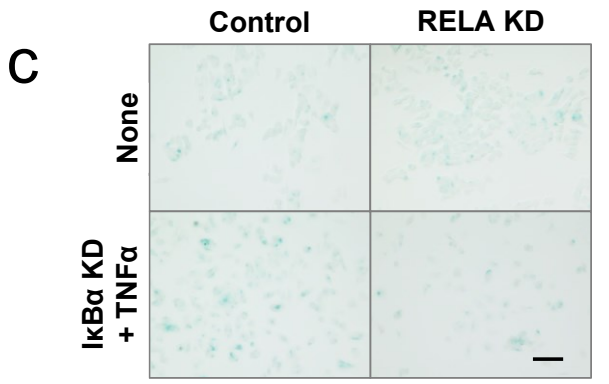

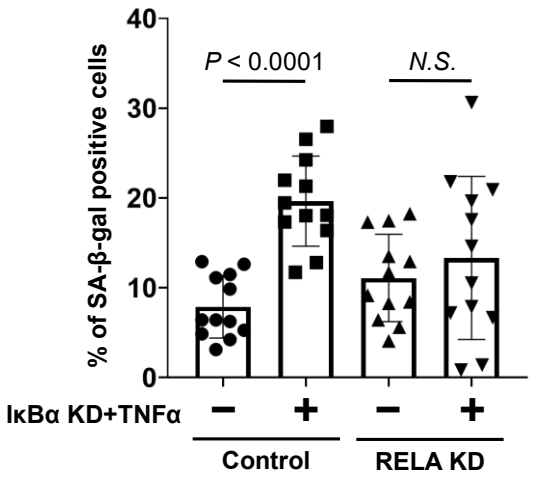

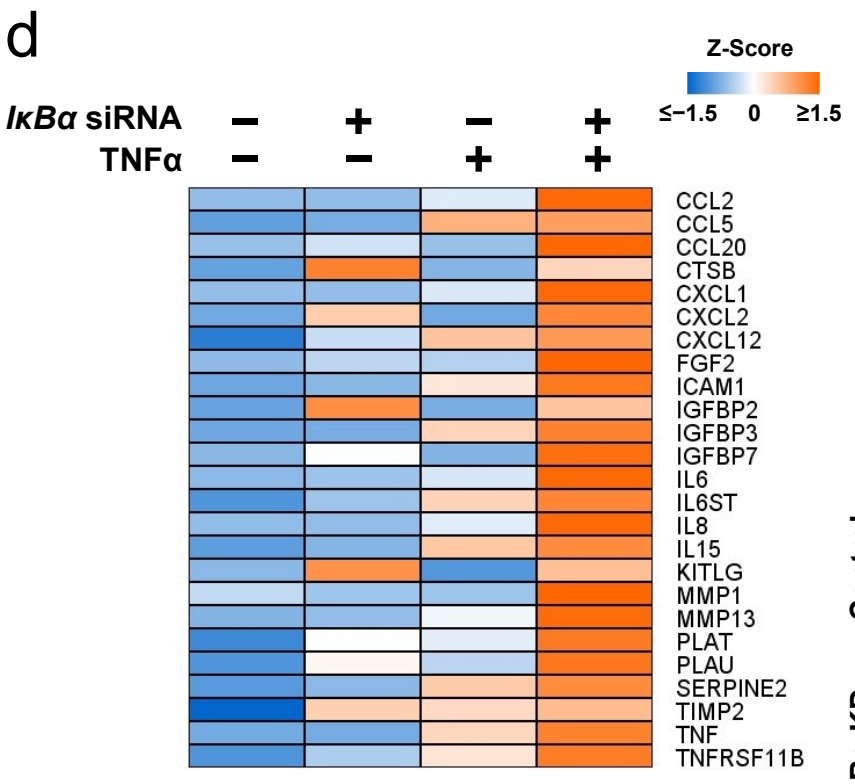

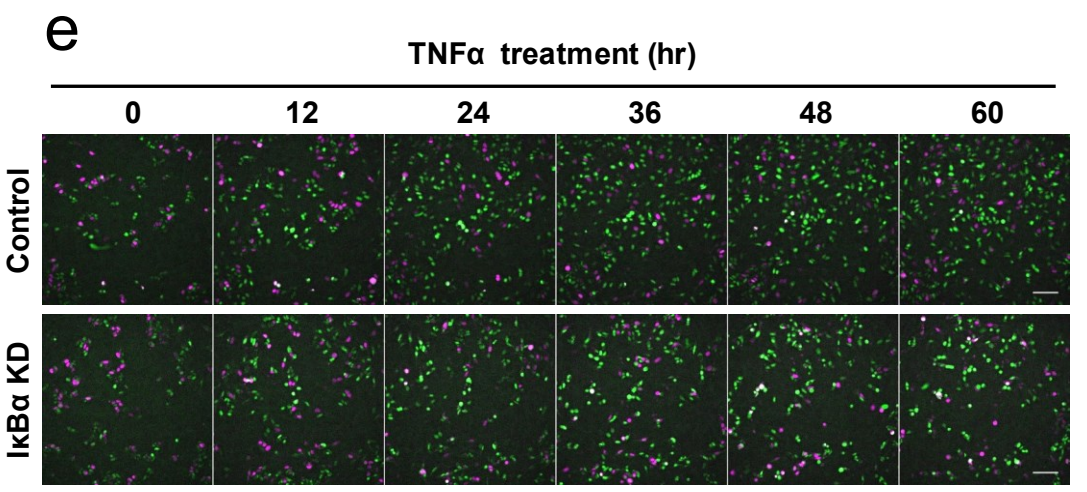

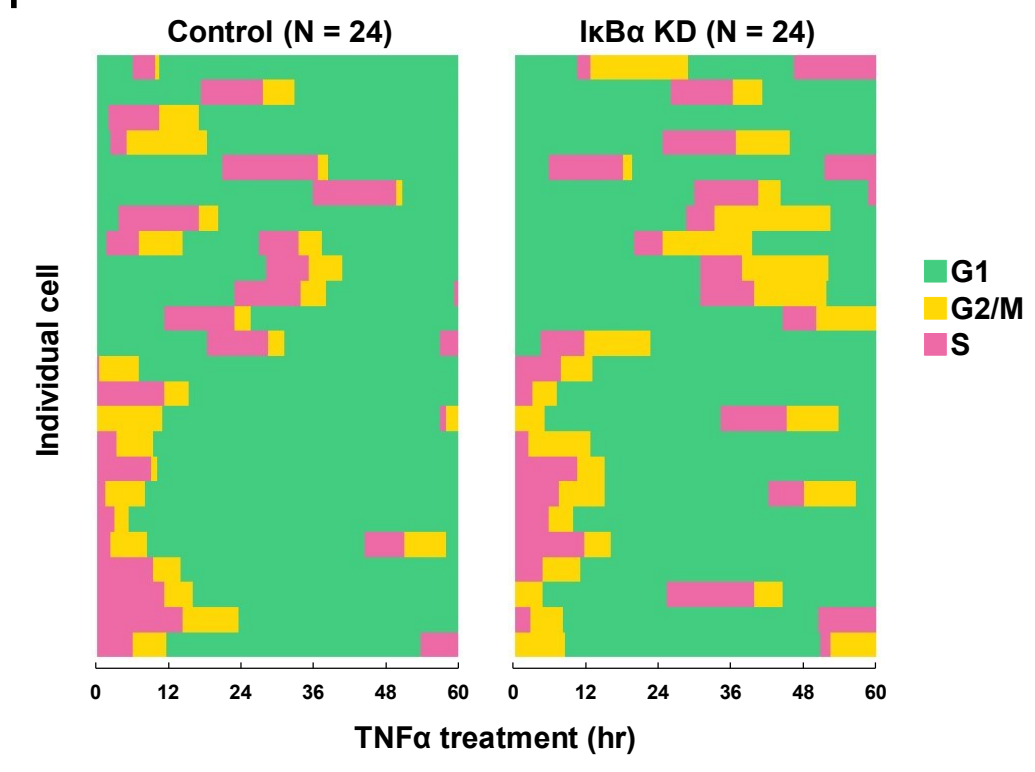

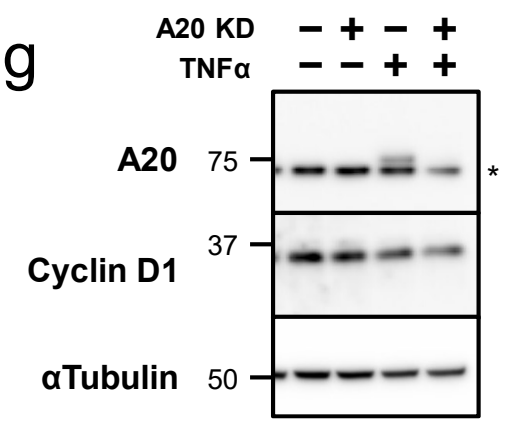

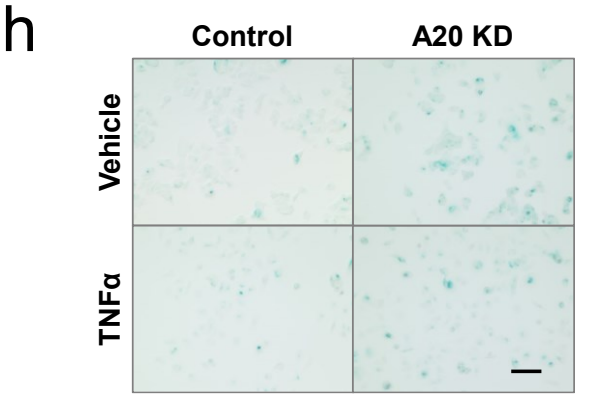

Extended Data Fig. 3

a

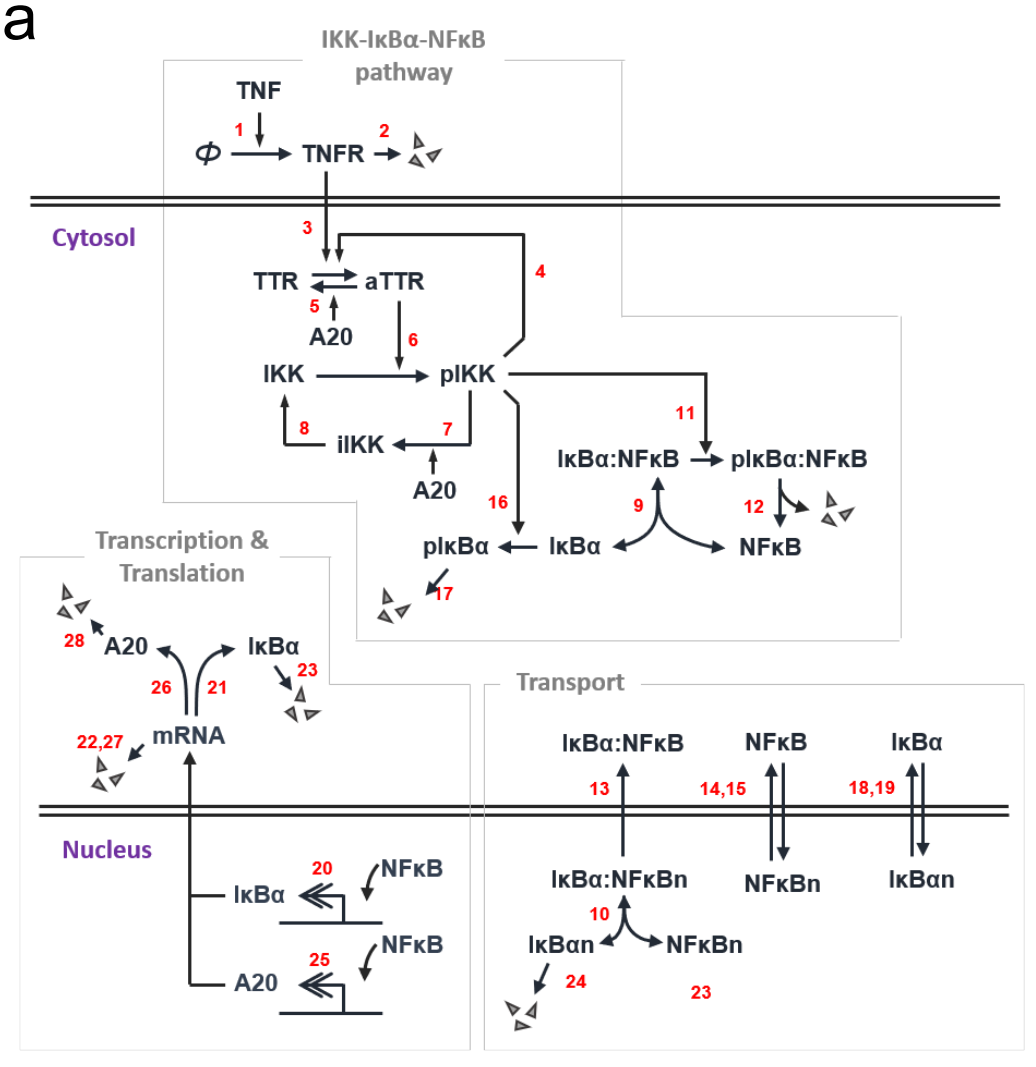

b

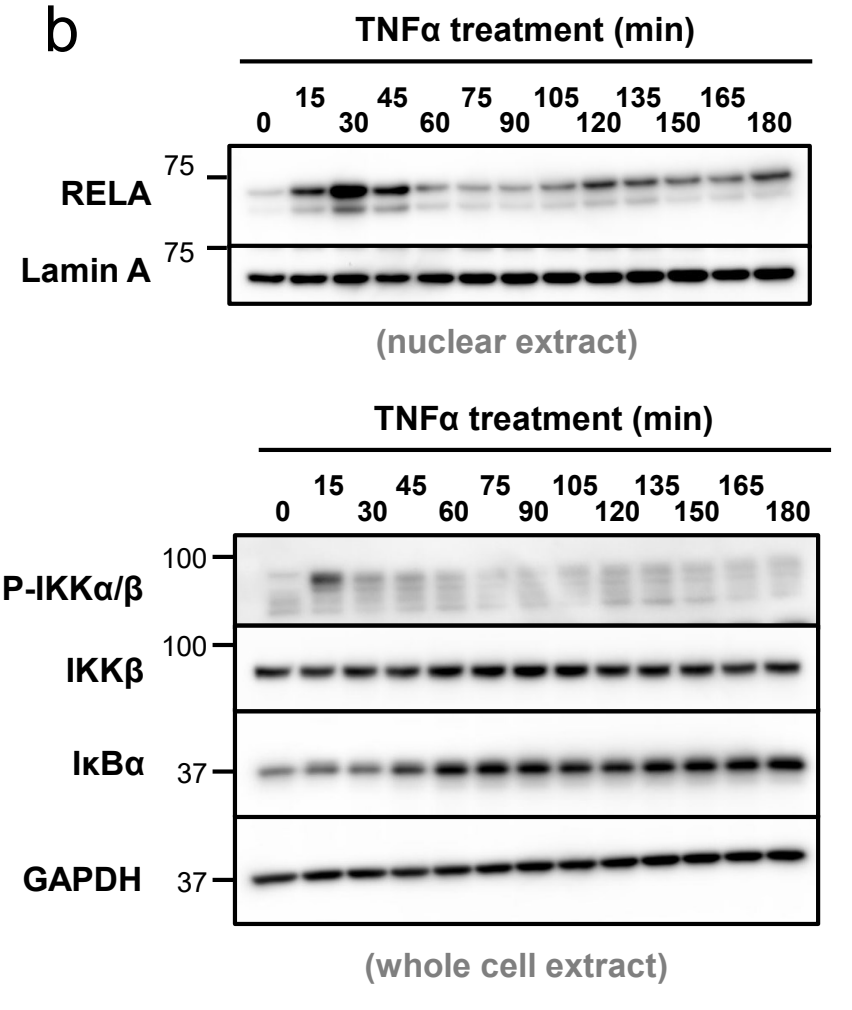

c

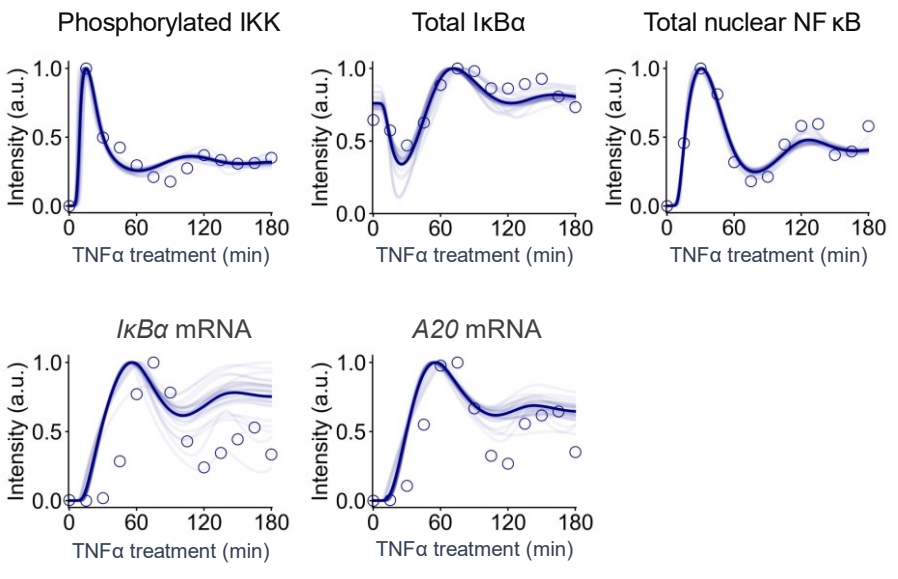

d

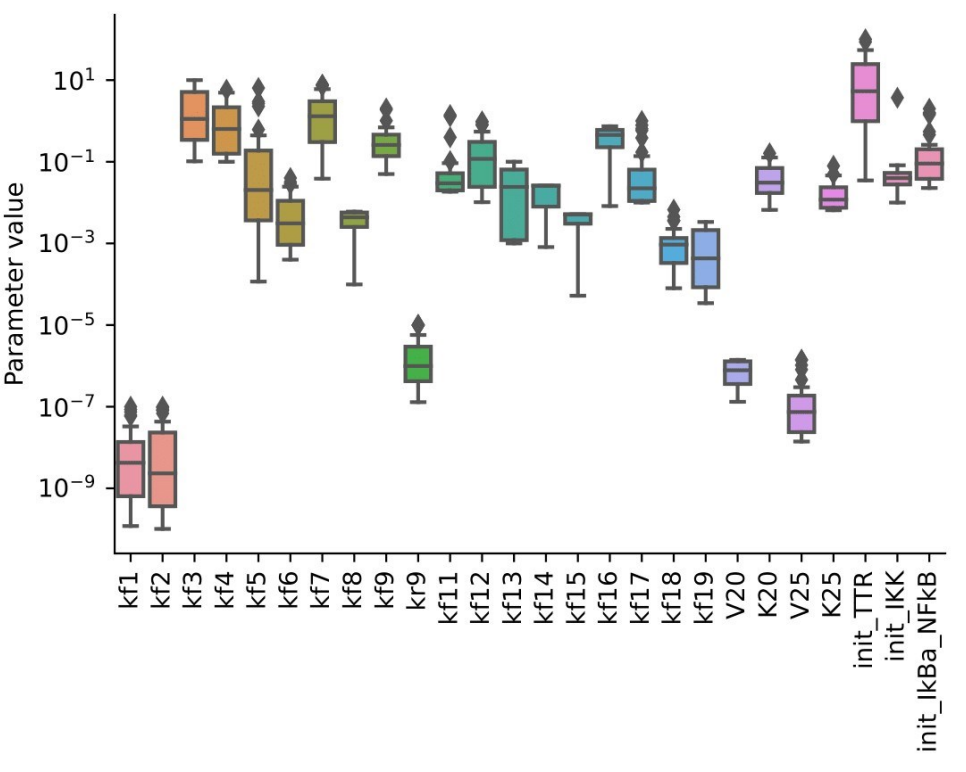

Extended Data Fig. 4

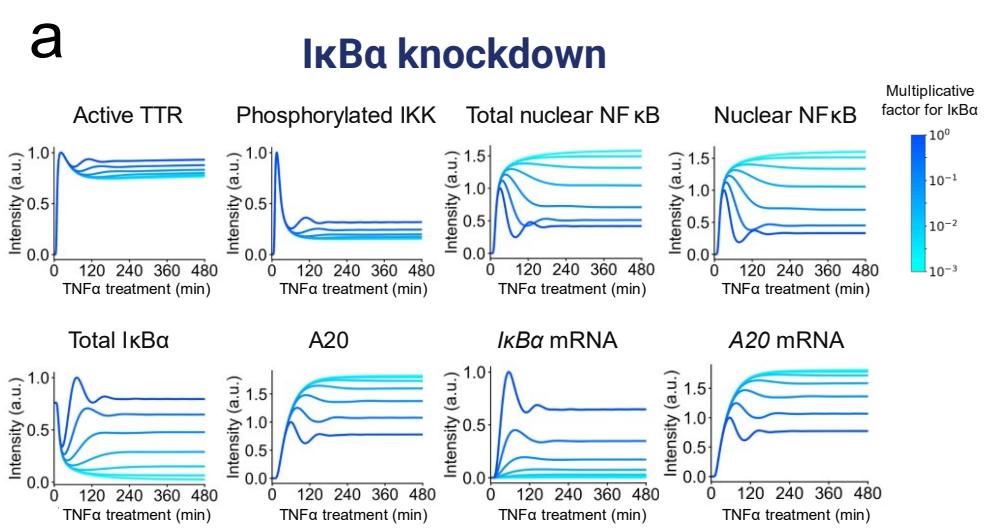

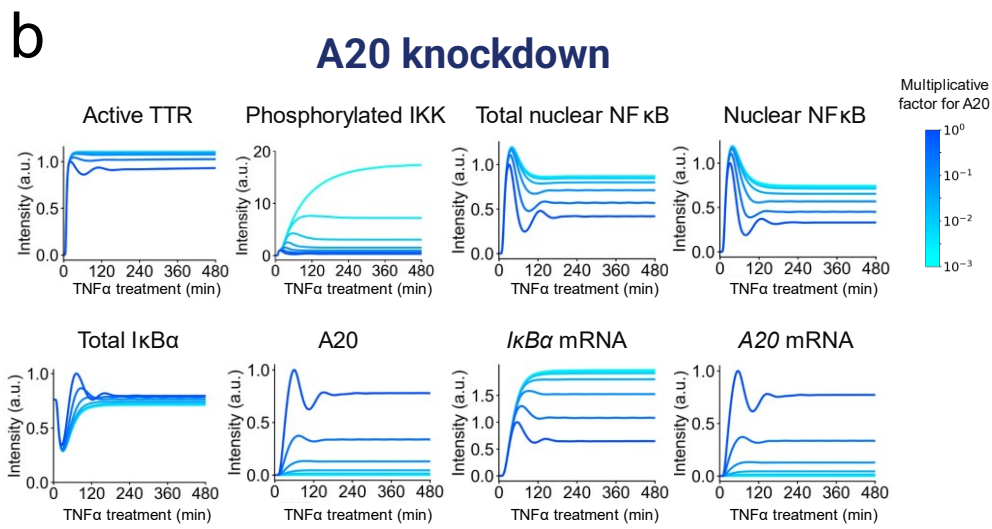

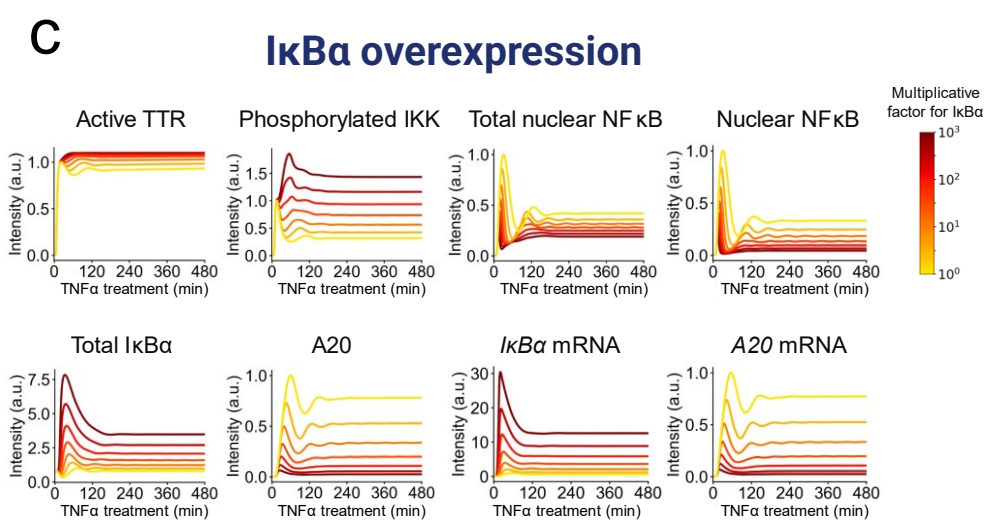

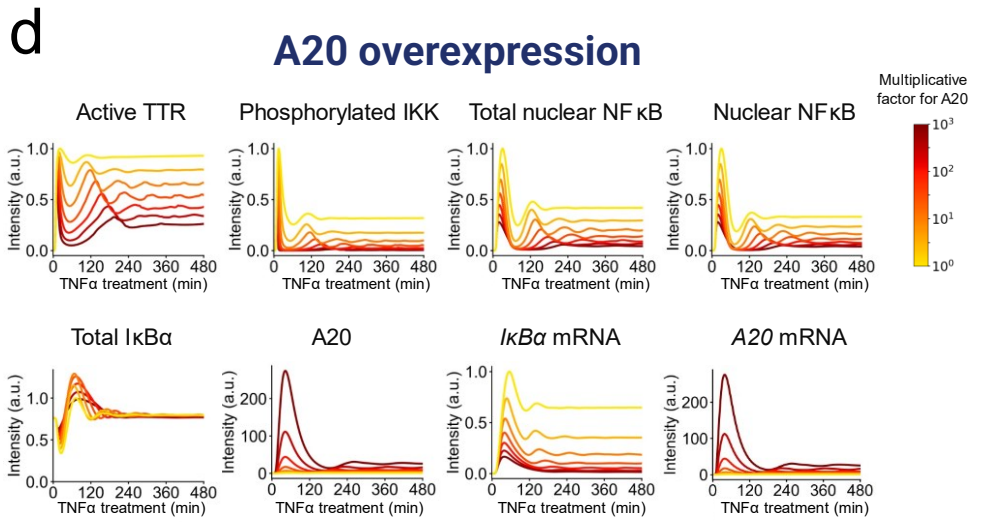

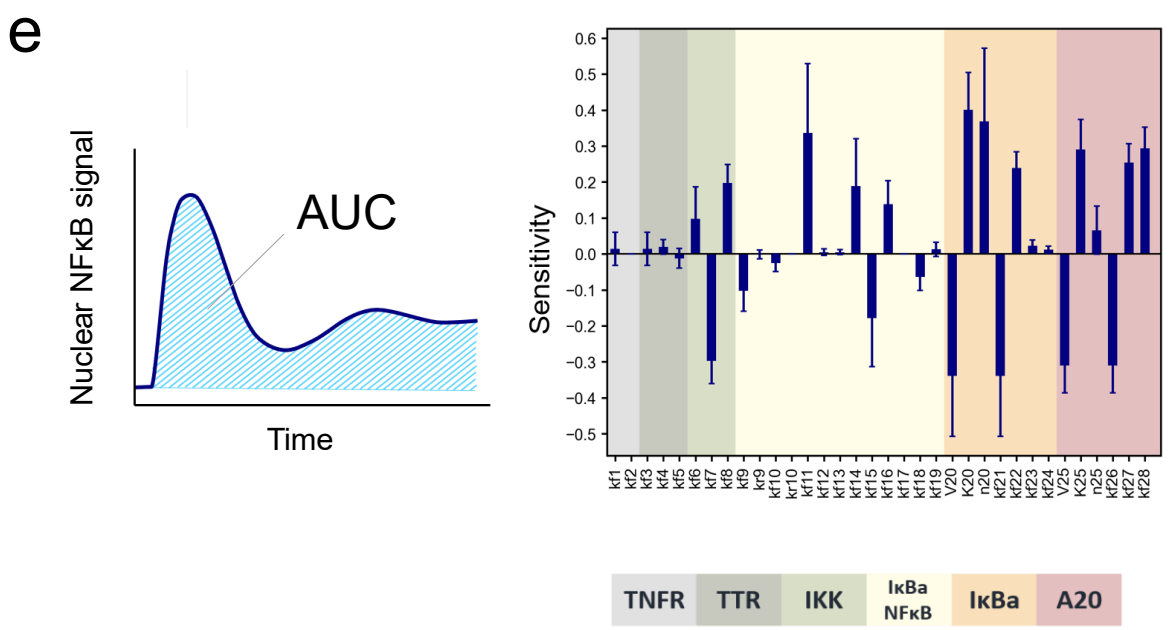

Extended Data Fig. 5

a

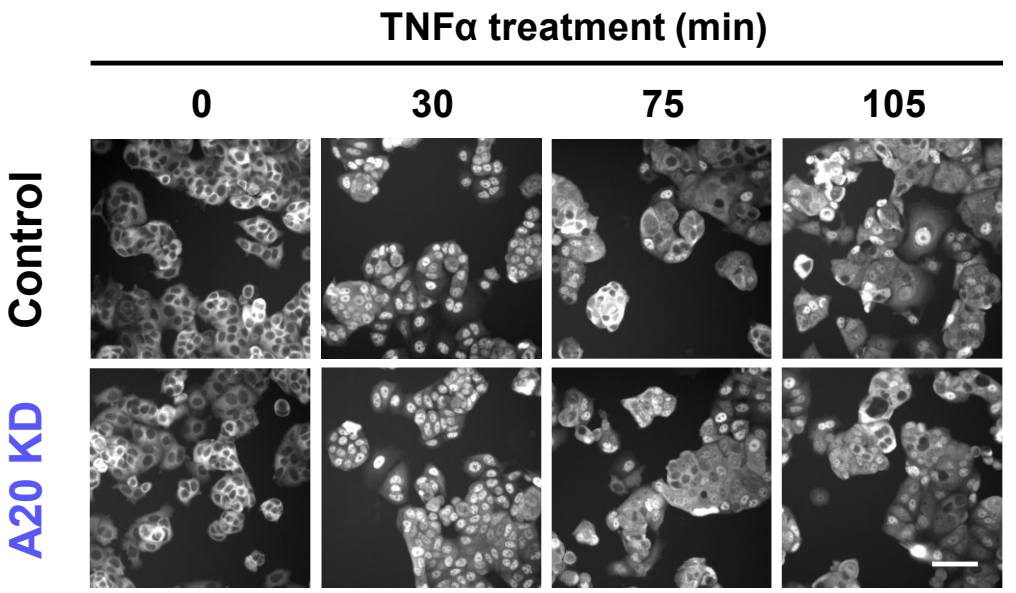

A20 OE + IκBα KD

b

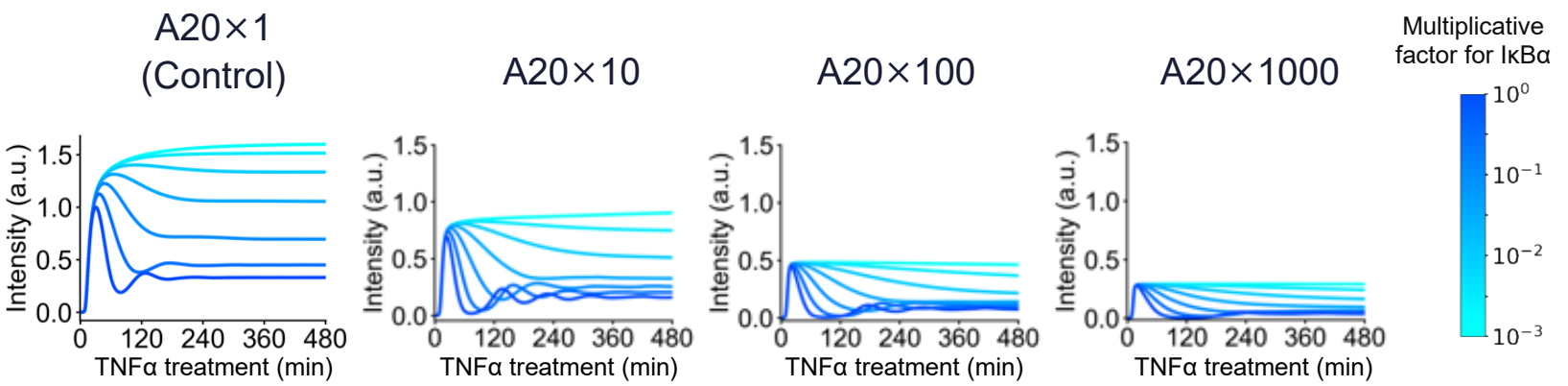

c

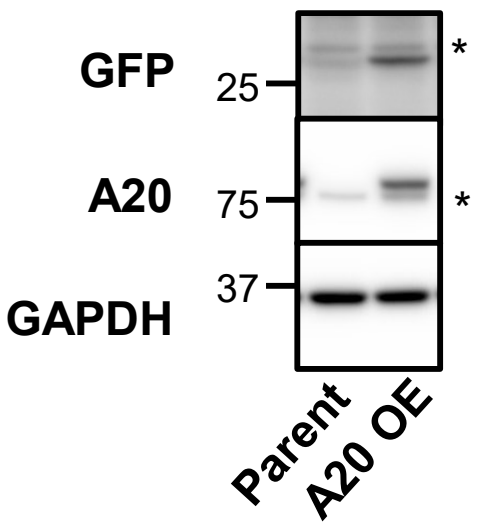

d

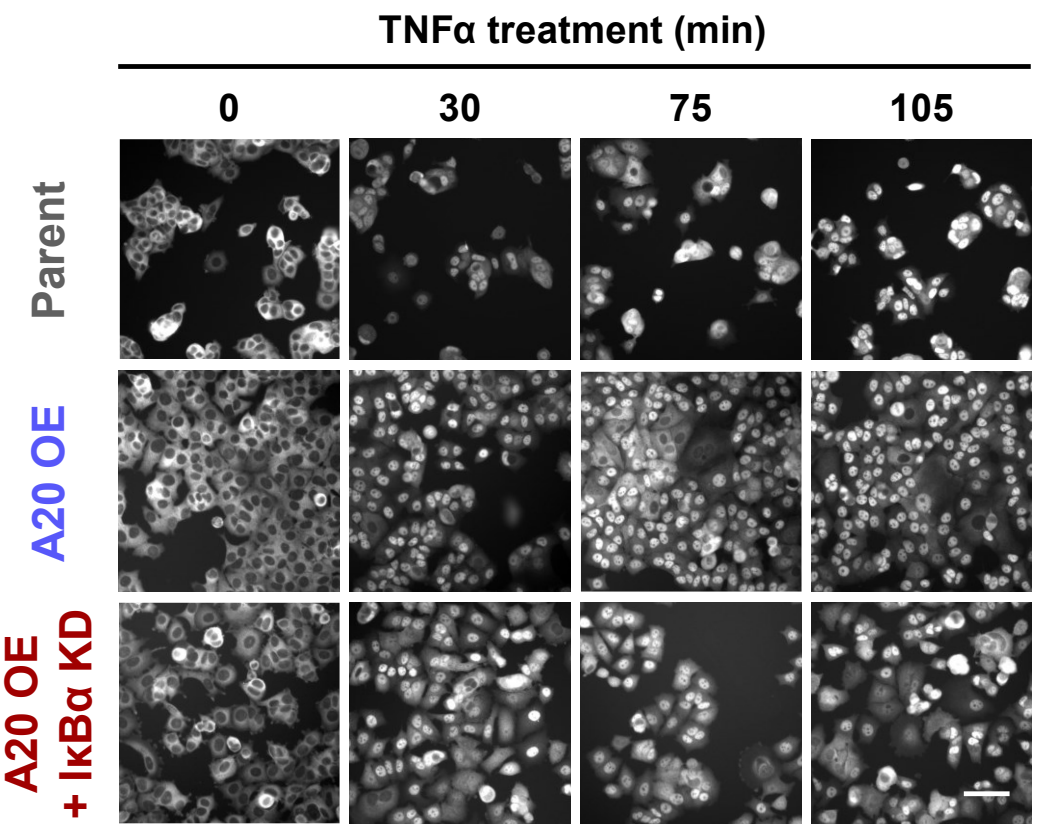

Extended Data Fig. 6

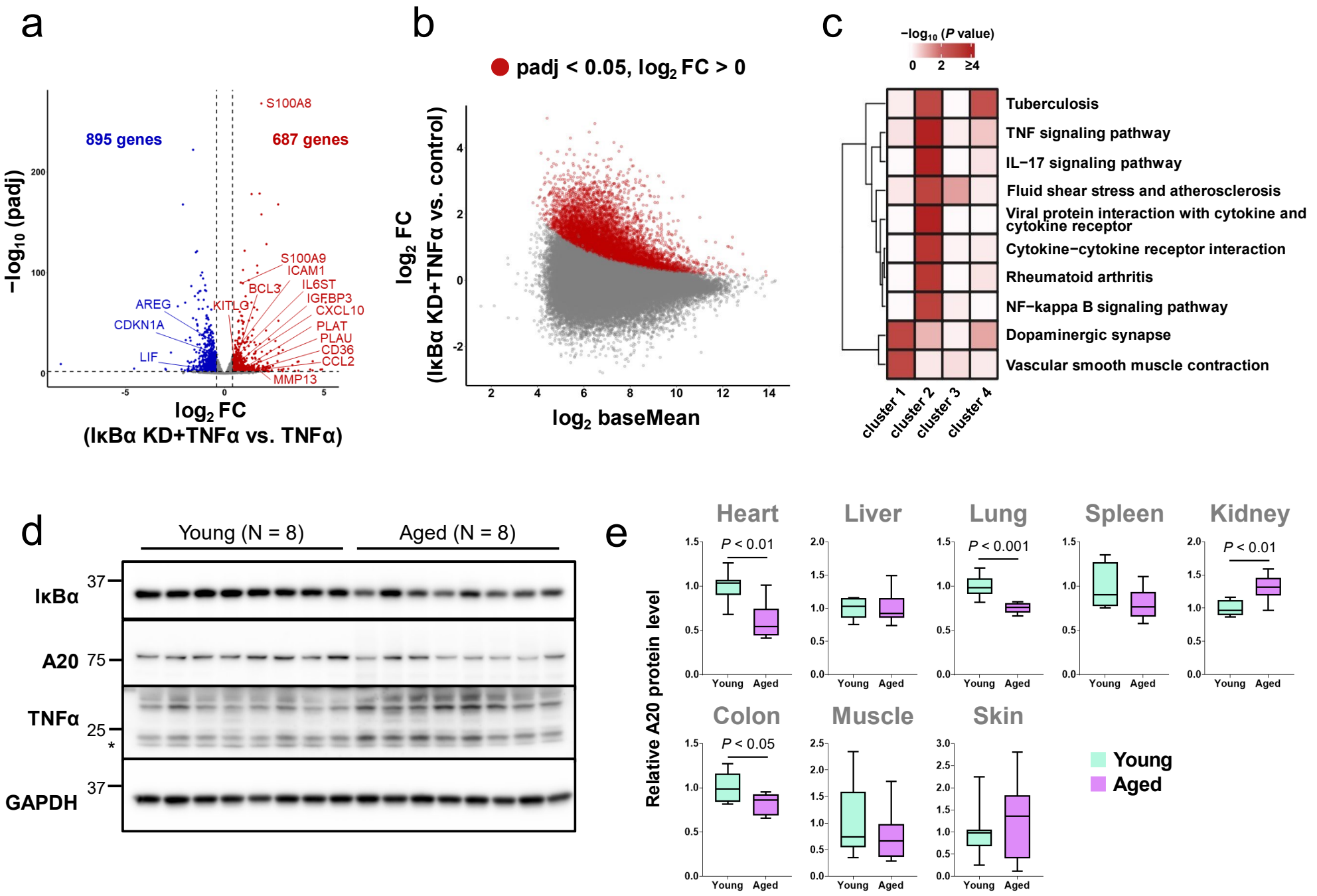

Extended Data Fig. 7

a

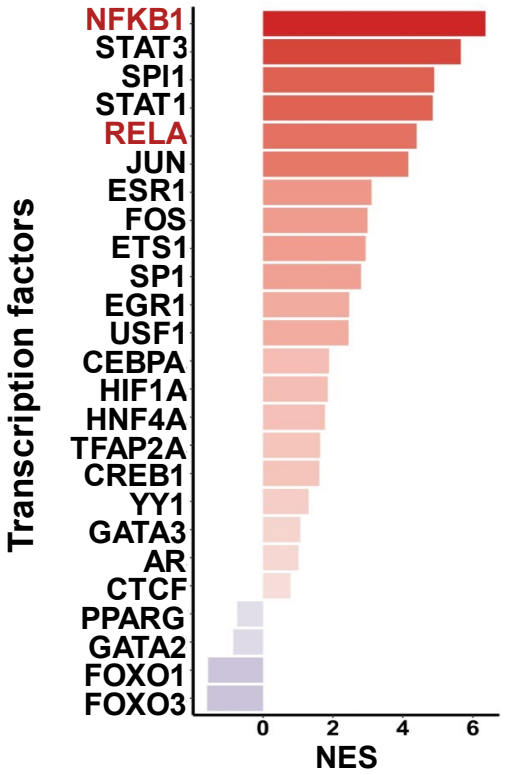

b

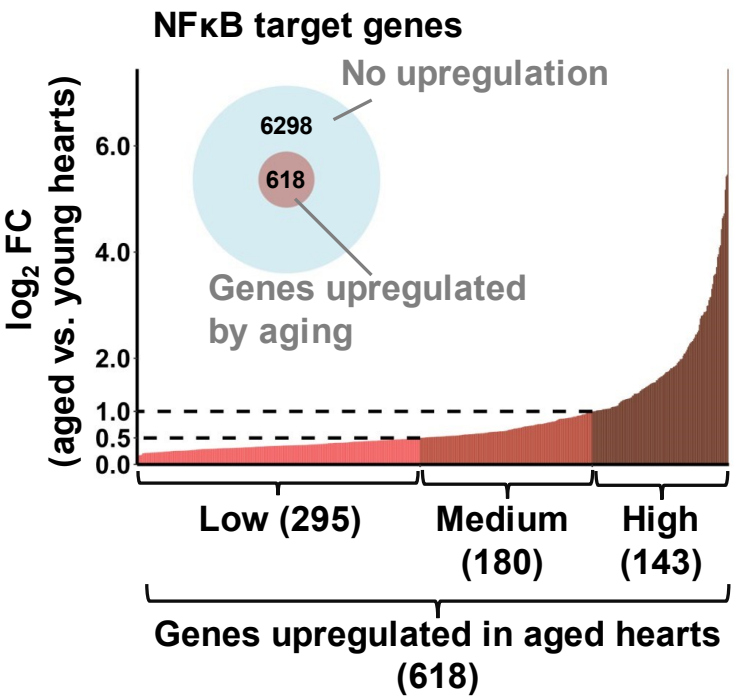

c

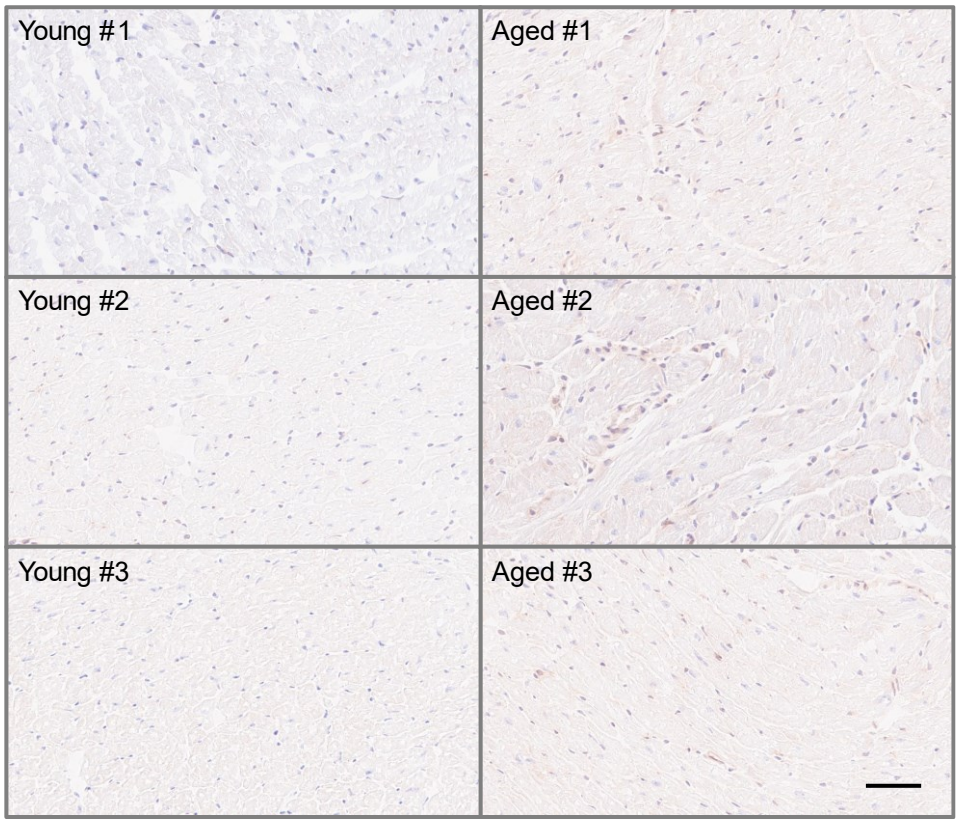

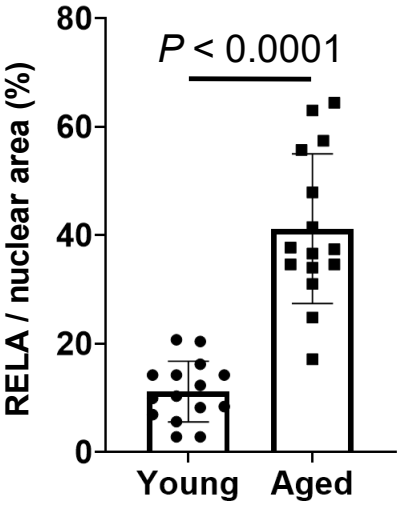

Extended Data Fig. 8

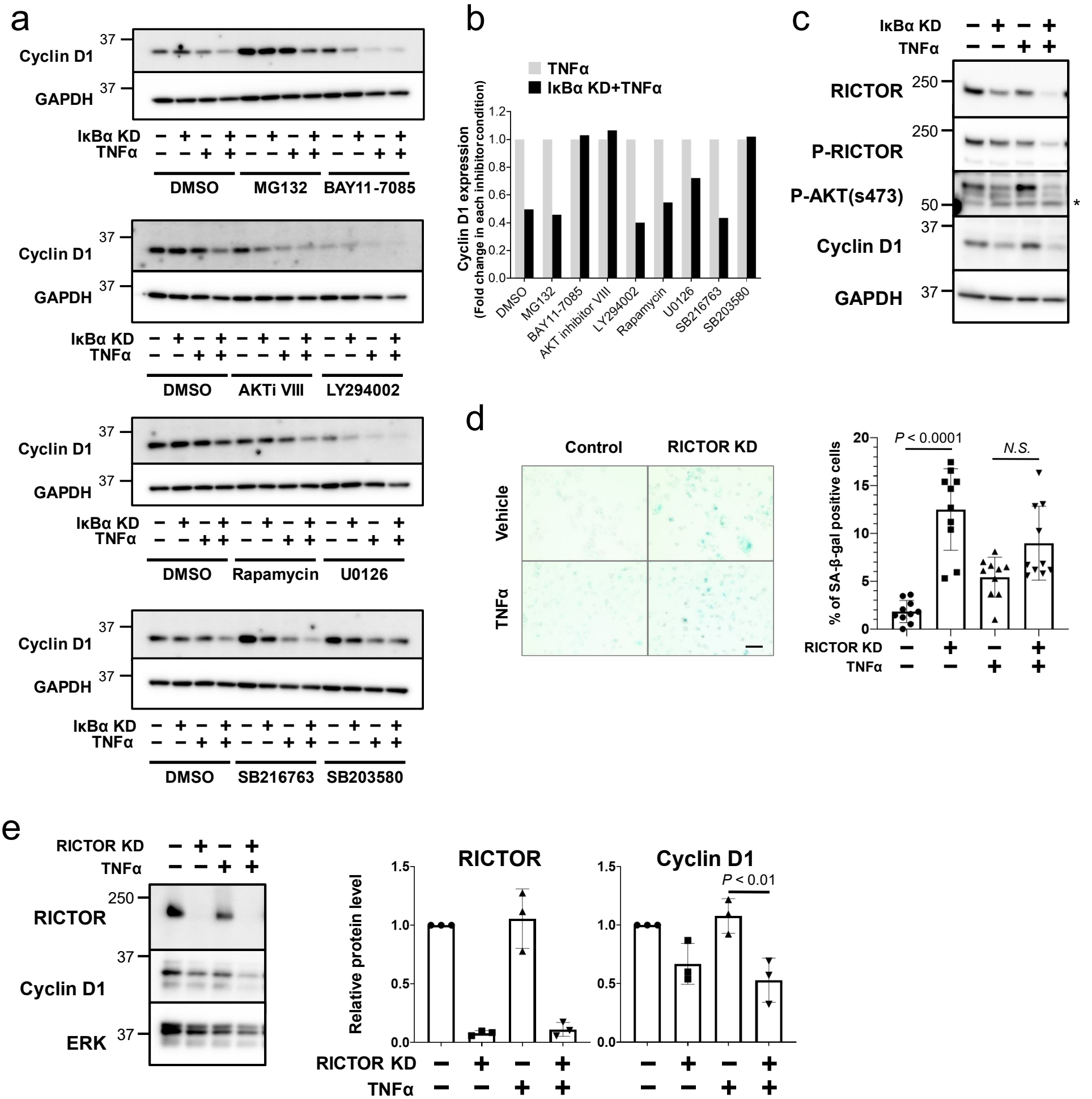

Extended Data Fig. 9

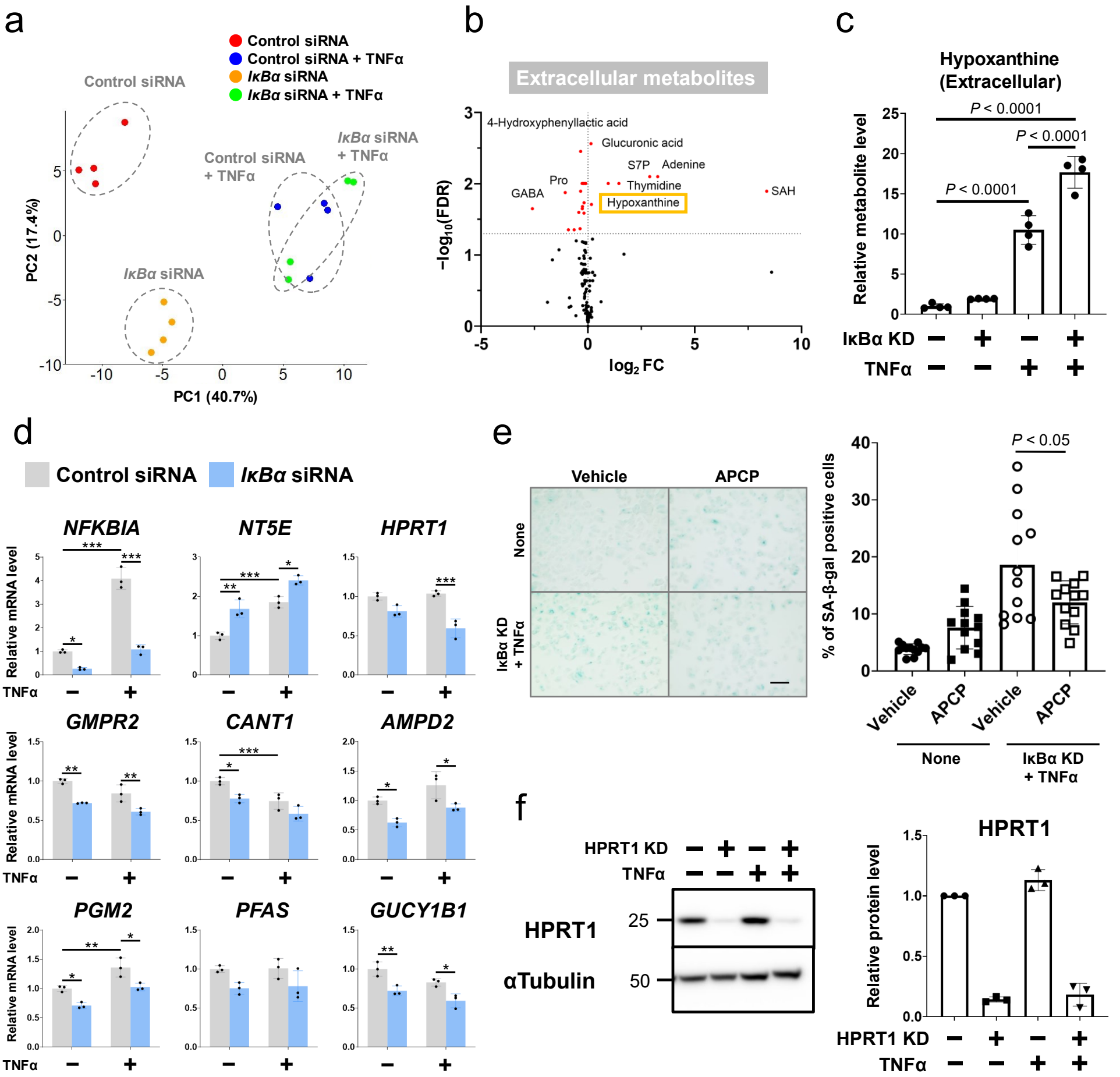
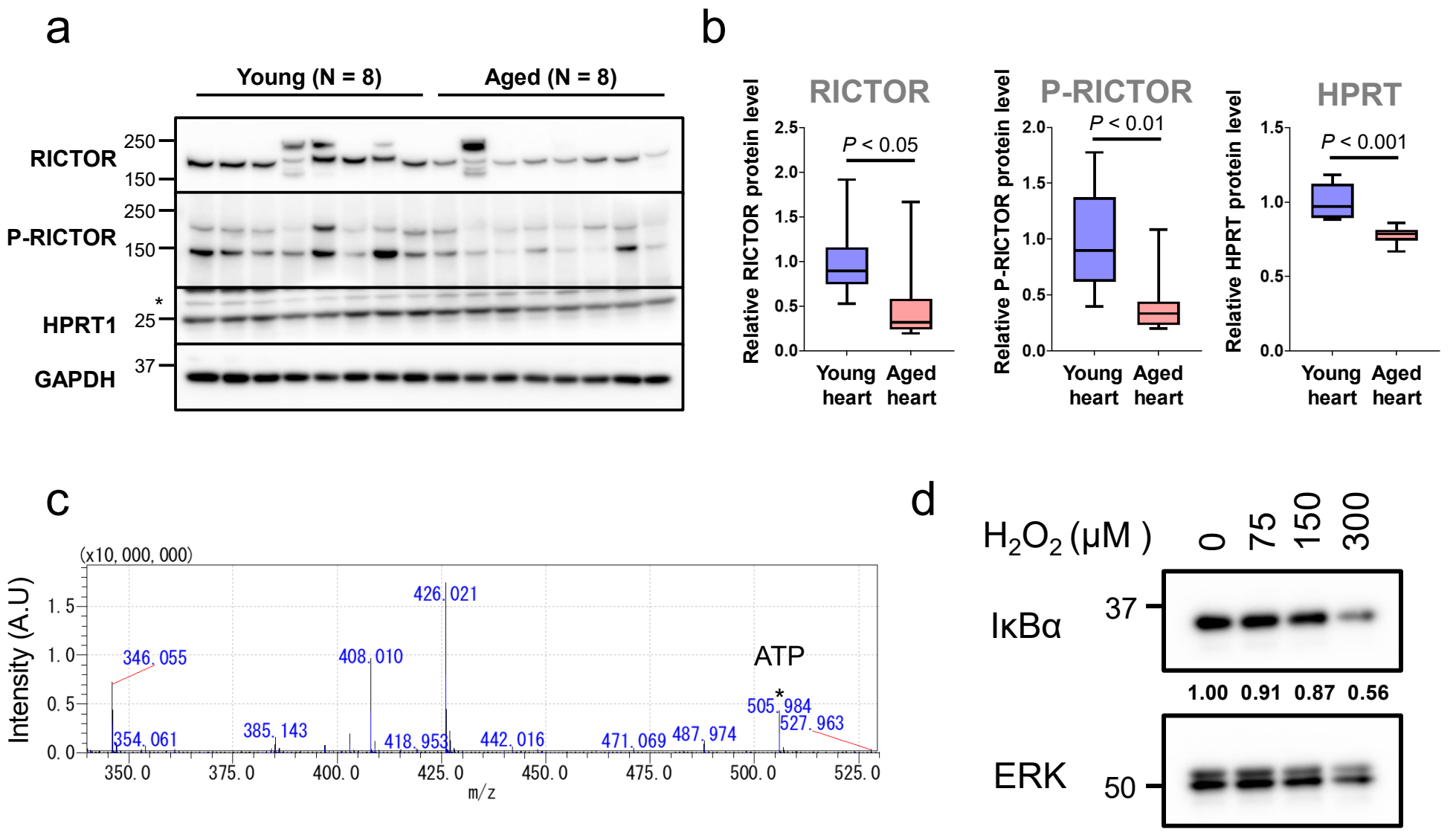
Extended Data Fig. 10